On the choice of closure complexity in anisotropic drag closures for filtered Two Fluid Models

*Jan Hendrik Cloete[1], Schalk Cloete[2], Stefan Radl[3], Shahriar Amini[1,2]**

1) Department of Energy and Process Engineering, Norwegian University of Science and Technology (NTNU), NO-7491 Trondheim, Norway

2) Flow Technology Research Group, SINTEF Industry, NO-7465 Trondheim, Norway

3) Institute of Process and Particle Engineering, Graz University of Technology, Inffeldgasse 13/III, 8010 Graz, Austria

*Corresponding author. Email: shahriar.amini@sintef.no

 Address: SINTEF Industry, S.P. Andersens vei 15 B, 7031 Trondheim, Norway, Phone: +47 46639721

Abstract

Filtered Two Fluid Models (fTFMs) aim to enable accurate industrial-scale simulations of fluidized beds by means of closures accounting for the effects of bubbles and clusters. The present study aims to improve anisotropic closures for the drift velocity, which is the primary sub-grid effect altering the filtered drag force, by deriving increasingly complex closures by considering additional independent variables (markers). Three different anisotropic closures, as well as an isotropic closure, are evaluated. A priori tests revealed a significant increase in the predictive capability of the closures as the complexity, in terms of the number of markers considered, increases. However, this improvement is relatively small when compared to the effect of considering anisotropy. Next, a posteriori tests were completed by comparing coarse-grid simulations of bubbling, turbulent and core-annular fluidization against benchmark resolved TFM simulations. This analysis shows good performance of all anisotropic closures, with negligible to minor effects of increasing the drag closure's complexity by considering additional markers. On the other hand, the isotropic closure lacks generality and shows poor grid independence behaviour. It is therefore concluded that it is essential to include important physical effects, such as anisotropy, in fTFM closures, while complexity in terms of the number of markers considered is of lesser importance.

Keywords: Fluidized bed, Computational Fluid Dynamics, Filtered Two Fluid Model, Coarse-grid simulations, Drag, Verification

1 Introduction

Fluidized beds are commonly used in many process industries due to their excellent mixing and mass and heat transfer capabilities. Simulation of these reactors by means of computational fluid dynamics (CFD) is particularly challenging due to the complex multiphase flow behaviour that fluidized beds exhibit, as well as the huge number of particles that typical industrial systems contain. A common solution is to simulate a fluidized bed by means of a Two Fluid Model (TFM). Here the solid particles are assumed to behave as a continuum, thereby reducing the computational cost by no longer requiring individual particles to be tracked. However, closures based on the Kinetic Theory of Granular Flow (KTGF) (Gidaspow et al., 1992; Lun et al., 1984) are required to model the effects of collisions and random translations of individual particles. A major limitation of the TFM is that it requires the solid clusters and gas bubbles, which are typical of fluidization and can occur on lengths scales as small as several particle diameters, to be resolved (Cloete et al., 2011; Cloete et al., 2015a, 2016c). This requires restrictively small grid cells to be used for accurate results, therefore studies using the TFM are generally limited to lab-scale studies (Bakshi et al., 2016; Cloete et al., 2016a; Cloete et al., 2015b; Cloete et al., 2013; Ellis et al., 2011; Hamidouche et al., 2019; Ostermeier et al., 2017; Tricomi et al., 2017).

The concept of a filtered TFM was proposed by Igci et al. (2008) as a possible method by which accurate results could be obtained for larger fluidized beds, while maintaining reasonable computational times by allowing coarse grid cells to be used. The basic idea is to develop closures for the effects of the sub-grid-scale clusters and bubbles that are not resolved in the coarse-grid simulations. The quantities that require closure can be identified by spatially averaging the governing equations of the TFM, and the necessary closures can be developed by filtering and subsequent analysis of data from resolved TFM simulations (Igci and Sundaresan, 2011), ideally informed by theoretical considerations (Schneiderbauer, 2017).

An approach based on the analysis of filtered resolved TFM data has been the most widely used in the fTFM literature, and several groups have reported closures based on this methodology (Gao et al., 2018; Igci and Sundaresan, 2011; Ozel et al., 2013). This is also the approach that has been followed previously by our research group (Cloete et al., 2017a, 2018a; Cloete et al., 2018b; Cloete et al., 2018c), and which will be followed in the present study. To derive closures from resolved TFM data, the data is generally filtered and then mapped out as a function of the size of the averaging region, referred to as the filter size, and other discretized independent variables, referred to as markers in the fTFM literature.

Previous research has revealed that for the large grid sizes that are typical of industrial-scale fluidized bed simulations (Cloete et al., 2016b), closures are necessary for the filtered drag force (Cloete et al., 2018a; Ozel et al., 2013; Schneiderbauer, 2017), the meso-scale interphase force (resulting from fluctuations in the gas pressure gradient) (Cloete et al., 2018a) and the meso-scale solids stresses (Cloete et al., 2018b; Ozel et al., 2013). Our previous papers have revealed the importance of accounting for anisotropy in these closures (Cloete et al., 2018a; Cloete et al., 2018b). However, despite the significant improvements that were made in these closures compared to the state-of-the-art, detailed 2D verification in the bubbling and turbulent fluidization regimes has still revealed significant differences between resolved TFM and coarse-grid fTFM simulations employing these closures.

The present study will therefore aim to further improve the accuracy of coarse grid fTFM simulations by focussing on the closure for the filtered drag force, which is generally accepted as the most important closure in fTFMs (Ozel et al., 2013; Schneiderbauer, 2017). The fTFM literature, as well as

the related work on sub-grid drag corrections using the EMMS methodology (Luo et al., 2017; Wang and Li, 2007; Yang et al., 2004), has generally accounted for meso-scale structures by multiplying the microscopic drag law evaluated at the filtered conditions with an isotropic drag correction factor. These closures are typically derived by considering the vertical direction data, assuming that the vertical drag is of much greater significance than the lateral drag forces. However, recent work has indicated that, although the vertical component of the drag is larger, the lateral contributions are clearly not insignificant and are drastically mispredicted by an isotropic fTFM drag closure based on the vertical direction data (Cloete et al., 2018a). The anisotropy in the sub-grid drag correction should therefore be accurately accounted for.

It has recently been shown that the drift velocity-based formulation of the filtered drag force (Ozel et al., 2013; Parmentier et al., 2012) offers clear benefits, primarily by making it simpler to account for effects due to drag anisotropy (Cloete et al., 2018a). It was also shown that the drift velocity consists of a part that is proportional to the filtered slip velocity in the direction considered, and another part that is aligned with the direction of gravity and independent of the filtered slip velocity. The drift velocity was then closed by means of a 2-marker closure with the filtered solids volume fraction as the first marker and the filtered slip velocity as the second marker, similar to previous studies (Gao et al., 2018; Milioli et al., 2013; Sarkar et al., 2016; Schneiderbauer and Pirker, 2014). In the present study, the importance of the filtered slip velocity as the second marker is first evaluated by deriving and testing a similar 1-marker anisotropic drift velocity-based closure. Next, it is revealed that the drift velocity can be redefined as a co-variance of the filtered gas velocity and filtered gas volume fraction. A complex 3-marker model is then derived and evaluated by adding a gradient product marker (GPM) as an additional independent variable, analogous to what was previously proposed for meso-scale solids stresses (Cloete et al., 2018b).

The results of this study are presented in the following order. First, the development of the 1-, 2- and 3-marker anisotropic closures is detailed. Second, these closures, as well as an older isotropic 2-marker closure (Cloete et al., 2018a; Cloete et al., 2018c) for perspective, are evaluated in an *a priori* manner by comparing resolved simulation data to model predictions. Third, the filtered drag force closures are tested in an *a posteriori* assessment by comparing resolved TFM simulation results to coarse grid simulations using the different fTFM closures. A wide range of fluidization regimes are considered to assess model generality. The main objective of the study is therefore to evaluate how increasing the number of independent variables in an fTFM drag closure affects the performance of coarse-grid fTFM simulations. This objective is pursued in a structured manner by considering a fixed fine-grid database and maintaining a similar closure structure when deriving closures of increasing levels of complexity. To conclude, the results are interpreted to help guide future fTFM development efforts.

2 Methodology

In this study, results from three sets of simulations are presented. The first simulation set consists of resolved TFM simulations in fully-periodic 2D domains, which are used for closure development. These simulations, as well as the data analysis using the open-source library, CPPPO (Municchi et al., 2016), is described in detail in our previous publications (Cloete et al., 2018a; Cloete et al., 2018b). Since exactly the same data set is used for the closures developed in our present paper, information regarding the periodic simulations is not repeated here. This section will therefore focus on describing the other two simulation sets, which are the resolved TFM and coarse-grid fTFM simulations for different fluidization regimes that are using to verify the developed closures.

2.1 Governing equations of the resolved TFM

This study employs a standard TFM in the resolved simulations, which will be described here briefly. For the interested reader, more details can be found in a previous study (Cloete et al., 2011).

The following continuity equations are solved for the gas and solids phases, respectively.

$$\frac{\partial}{\partial t}\left(\alpha_g \rho_g\right) + \nabla \cdot \left(\alpha_g \rho_g \vec{v}_g\right) = 0 \qquad \text{Equation 1}$$

$$\frac{\partial}{\partial t}\left(\alpha_s \rho_s\right) + \nabla \cdot \left(\alpha_s \rho_s \vec{v}_s\right) = 0 \qquad \text{Equation 2}$$

It can be noted that the volume fractions of the two phases sum to unity. The following momentum conservation equations are also solved.

$$\frac{\partial}{\partial t}\left(\alpha_g \rho_g \vec{v}_g\right) + \nabla \cdot \left(\alpha_g \rho_g \vec{v}_g \vec{v}_g\right) = -\alpha_g \nabla p + \nabla \cdot \bar{\bar{\tau}}_g + \alpha_g \rho_g \vec{g} + K_{sg}\left(\vec{v}_s - \vec{v}_g\right) \qquad \text{Equation 3}$$

$$\frac{\partial}{\partial t}\left(\alpha_s \rho_s \vec{v}_s\right) + \nabla \cdot \left(\alpha_s \rho_s \vec{v}_s \vec{v}_s\right) = -\alpha_s \nabla p - \nabla p_s + \nabla \cdot \bar{\bar{\tau}}_s + \alpha_s \rho_s \vec{g} + K_{sg}\left(\vec{v}_g - \vec{v}_s\right) \qquad \text{Equation 4}$$

In both momentum equations, the last term represents the momentum transfer rate due to drag, which is closed by the Huilin-Gidaspow model (Huilin and Gidaspow, 2003) in this study. In the solids momentum equation, the solids stresses (contained in the second and third terms on the right-hand side) require closures for the granular pressure (Lun et al., 1984), as well as for the granular shear (Gidaspow et al., 1992) and bulk (Lun et al., 1984) viscosities as predicted by the KTGF. Additionally, closures (Johnson and Jackson, 1987; Schaeffer, 1987) are required to account for the effects of prolonged frictional contacts between the particles, since a previous study indicated that including frictional stresses has a significant influence on the qualitative behaviour of fTFM closures (Cloete et al., 2017a).

In the kinetic theory stresses, information about the granular temperature, a measure of the random fluctuating energy of the particles, is required. For this, the following transport equation is solved.

$$\frac{3}{2}\left[\frac{\partial}{\partial t}\left(\alpha_s \rho_s \Theta_s\right) + \nabla \cdot \left(\alpha_s \rho_s \vec{v}_s \Theta_s\right)\right] = \left(-p_s \bar{\bar{I}} + \bar{\bar{\tau}}_s\right) : \nabla \vec{v}_s + \nabla \cdot \left(k_{\Theta_s} \nabla \Theta_s\right) - \gamma_{\Theta_s} + \phi_{gs} \qquad \text{Equation 5}$$

Here, from left to right, the terms on the right-hand side of the equation are: the generation of granular temperature due to the solids stresses, the granular conductivity (Gidaspow et al., 1992), the dissipation of granular temperature due to inelastic collisions (Lun et al., 1984) and the dissipation due to the interphase drag (Gidaspow et al., 1992).

2.2 Governing equations of the filtered TFM

The filtered versions of the equations presented in section 2.1 can be derived by applying a spatial average, and then re-arranging by defining phase-weighted averages and fluctuating quantities. This is detailed in previous work (Cloete et al., 2018a; Cloete et al., 2018b) and is therefore not repeated here in detail. However, it should be noted that, in our present study, the fluctuating component is defined relative to the average (filtered) value that is fixed in the filter region. This is different to the definition common in single-phase LES (where the fluctuating component is defined relative to the local average). Thus, our filtered equations do not contain Leonard and cross terms, since these terms are lumped into our terms that account for spatial fluctuations. Most importantly, it means that, in the present work, the following identities hold: $\rho_g \overline{\alpha_g \vec{v}_g{}'' \vec{v}_g{}''} = \overline{\rho_g \alpha_g \vec{v}_g \vec{v}_g} - \rho_g \overline{\alpha_g} \tilde{\vec{v}}_g \tilde{\vec{v}}_g$, $\rho_s \overline{\alpha_s \vec{v}_s{}'' \vec{v}_s{}''} = \overline{\rho_s \alpha_s \vec{v}_s \vec{v}_s} - \rho_s \overline{\alpha_s} \tilde{\vec{v}}_s \tilde{\vec{v}}_s$ and $\overline{\alpha_g{}' \nabla p'} = \overline{\alpha_g \nabla p} - \overline{\alpha_g} \nabla \bar{p} = -\overline{\alpha_s{}' \nabla p'} = -(\overline{\alpha_s \nabla p} - \overline{\alpha_s} \nabla \bar{p})$. The interested

4

reader may see Appendix A.1 in our previous publication (Cloete et al., 2018a) for a more detailed explanation.

The following discussion is limited to the filtered gas and solids momentum conservation equations, since these equations contain all the terms that require closure to simulate the hydrodynamics of fluidized beds using industrially relevant grid sizes.

$$\frac{\partial}{\partial t}\left(\rho_g \overline{\alpha_g}\widetilde{\vec{v}_g}\right) + \nabla \cdot \left(\rho_g \overline{\alpha_g}\widetilde{\vec{v}_g}\widetilde{\vec{v}_g}\right)$$
$$= -\overline{\alpha_g}\nabla \bar{p} - \nabla \cdot \left(\rho_g \overline{\alpha_g \vec{v}_g{}''\vec{v}_g{}''}\right) + \nabla \cdot \overline{\overline{\bar{\tau}}}_g + \overline{\alpha_g}\rho_g \vec{g} + \overline{K_{sg}(\vec{v}_s - \vec{v}_g)}$$
$$- \overline{\alpha_g{}'\nabla p'}$$

Equation 6

$$\frac{\partial}{\partial t}\left(\rho_s \overline{\alpha_s}\widetilde{\vec{v}_s}\right) + \nabla \cdot \left(\rho_s \overline{\alpha_s}\widetilde{\vec{v}_s}\widetilde{\vec{v}_s}\right)$$
$$= -\overline{\alpha_s}\nabla \bar{p} - \nabla \bar{p}_s - \nabla \cdot \left(\rho_s \overline{\alpha_s \vec{v}_s{}'\vec{v}_s{}'}\right) + \nabla \cdot \overline{\overline{\bar{\tau}}}_s + \overline{\alpha_s}\rho_s \vec{g}$$
$$+ \overline{K_{gs}(\vec{v}_g - \vec{v}_s)} - \overline{\alpha_s{}'\nabla p'}$$

Equation 7

In both equations, all the required information is available in the coarse-grid simulations for both terms on the left-hand side, the term due to the resolved gas pressure gradient (first term on the right-hand side) and the term due to gravity (fourth term on the right-hand side of Equation 6 and fifth term on the right-hand side of Equation 7). All other terms require closure. The filtered micro-scale gas phase stresses (third term on the right-hand side of Equation 6) are generally evaluated at their filtered values (Pope, 2000; Schneiderbauer, 2017). The meso-scale gas stresses (second term on the right-hand side of Equation 6) can safely be neglected for gas-particle flows (Milioli et al., 2013). This is due to the large density difference of the phases.

Considering the filtered microscopic solids stresses (second and fourth terms on the right-hand side of Equation 7), the kinetic theory contributions are approximated by evaluating the closures used in the resolved TFM at their filtered values. The filtered granular temperature is approximated based on the unfiltered granular temperature transport equation, which was previously shown to be sufficient for the filter sizes considered here (Cloete, 2018). The filtered frictional stresses are closed based on the results of a previous study (Cloete et al., 2018b).

Anisotropic closures are used for the meso-scale solids stresses (Cloete et al., 2018b) (third term on the right-hand side of Equation 7) and the meso-scale interphase force (Cloete et al., 2018a) (last term on the right-hand side of Equation 6 and Equation 7). The present study will focus on the remaining unclosed term that appears in both filtered momentum equations, the filtered drag force (second last term in both equations).

2.3   TFM and fTFM solver

Both resolved and coarse-grid fTFM simulations are perform in FLUENT 16.2. The phase-coupled SIMPLE algorithm (Patankar, 1980) is used for pressure-velocity coupling, and all other equations are discretized based on the QUICK scheme (Leonard and Mokhtari, 1990). The second-order implicit scheme is used for time discretization, since this has previously been found to be a requirement for time step independent solutions in dilute flow (Cloete et al., 2011). The terms that require closure in the fTFM were included as source terms in the momentum equations by using User-defined Functions (UDFs) in FLUENT.

2.4 Geometry and boundary conditions of the verification simulations

Three verification cases were considered to evaluate the developed fTFM closures over a range of fluidization conditions. Based on the correlations of Bi and Grace (1995), the cases were chosen at the geometric centre of the bubbling regime, at the start of the turbulent regime and at the geometric centre of the core-annular transport regime. The gas fluidization velocity considered in each case is listed in Table 1.

Table 1 - Summary of the three verification cases considered in this study

Verification case	Gas inlet velocity (m/s)	Height (m)	Width (m)
Bubbling	0.086	0.80	0.48
Turbulent	1.171	1.20	0.32
Core-annular	4.229	1.60	0.24

The simulations were performed in rectangular 2D domains, with the aspect ratio increasing with increasing fluidization velocity, as shown in Table 1. The choice of 2D simulations is justified based on previous findings that fTFM closures derived from 2D and 3D resolved TFM simulations are qualitatively similar (Igci et al., 2008) and that fTFM closures derived in 2D can perform well in validation against 3D experimental data (Cloete et al., 2018c). Developing and verifying fTFM closures in 2D therefore speeds up the development of the closures by allowing multiple resolved simulations to performed at different conditions, and by allowing simulation of larger domains that are more representative of industrial-scale systems. The resulting closures can then either be used directly in coarse-grid 3D simulations or, in the future, the lessons learned from 2D data can be applied to datasets from resolved TFM simulations in 3D.

For all three cases the bottom boundary was set as an inlet with a uniform gas velocity. The side boundaries are set as walls with a no-slip boundary conditions for the gas and a free-slip boundary condition for the solids. It can be noted that although a partial-slip boundary conditions would be more realistic for the solids, such a boundary condition would require an additional closure for the filtered shear stress at the walls. Developing such a closure is outside the scope of the present study, therefore a free-slip boundary conditions is deemed sufficient for verification purposes. The top boundary is set as a pressure outlet. For the bubbling and turbulent cases the domain-averaged solids volume fraction inside the fluidized bed is initialized as 0.25 and 0.05, respectively. A small amount of solids reach the outlet in the turbulent case. In order to maintain a constant solids inventory, the outgoing solids are uniformly reintroduced at the inlet. For the core-annular case, solids are injected at a mass flux of $150 \frac{kg}{m^2 s}$ at a port in each of the walls. These ports are located 4 cm above the inlet boundary and are 4 cm wide.

In the resolved TFM simulations, a uniform grid with a size of 0.625 mm (8.33 d_p) is used, which is the same as what is used in the fully-periodic resolved TFM simulations used to generate data for developing the closures in this study. In the coarse grid simulations, grid sizes of 10mm (133 d_p or 2.06 times the characteristic length), 20mm (267 d_p or 4.12 times the characteristic length) and 40 mm (533 d_p or 8.23 times the characteristic length) are considered, where the characteristic length scale is chosen as the particles' relaxation length, v_t^2/g. Assuming perfect parallelization of the solver, the coarse-grid simulations will lead to approximately 3-5 orders of magnitude reduction in computational time in 2D, and approximately 5-7 orders of magnitude in 3D.

After initialization, the simulations are run for sufficient time to reach a pseudo-state state, which is determined by monitoring domain-averaged quantities of the phase velocities and the solids volume

fraction in the core-annular case. The simulations are then time-averaged to allow comparison between the resolved TFM and coarse-grid fTFM simulations. Time-averaging is performed for 30 s in the bubbling case and 15 s for the turbulent and core-annular cases.

To conclude this section, Figure 1 visually compares the three verification cases that are considered by showing instantaneous solids volume fractions contours from the resolved TFM simulations.
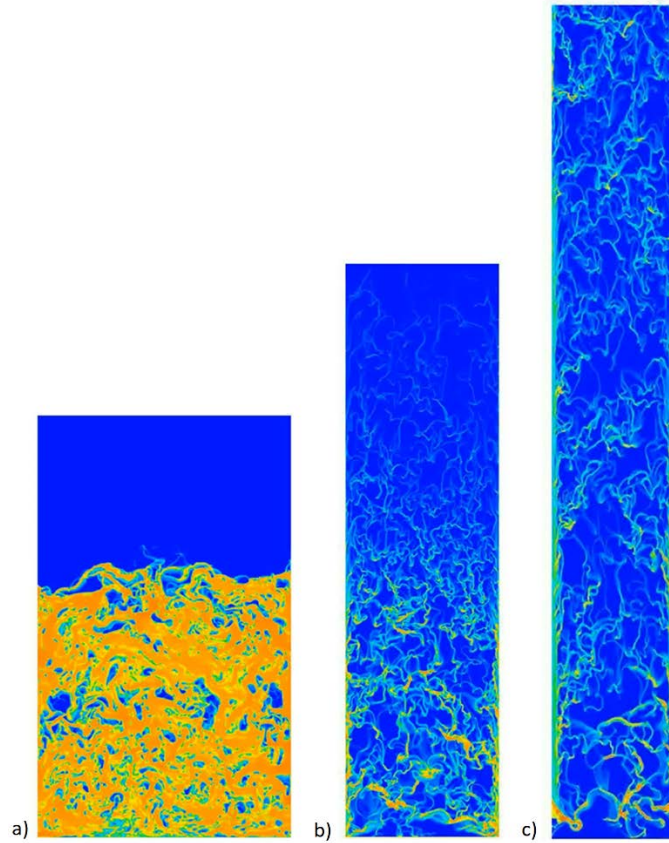

Figure 1 - Instantaneous solids volume fraction contours in a) the bubbling case, b) the turbulent case and c) the core-annular case. Blue indicates that no solids are present and red indicates maximum packing.

2.5   Material properties of the verification simulations

The particle and gas properties considered in the verification simulations are summarised in Table 2. It can be noted that these are exactly the same conditions that were considered in the fully-periodic resolved TFM simulations that are used to derive the fTFM closures. The scope of the present study is therefore limited to investigating how the accuracy of fTFM closures can be improved for a specific set of particle and fluid properties. Scaling of the closures to different conditions will be considered in a future study.

Table 2 - The material properties used in this study

d_p	Particle diameter	75×10^{-6} m
ρ_s	Particle density	1500 kg/m^3
ρ_g	Gas density	1.3 kg/m^3
μ_g	Gas viscosity	1.8×10^{-5} kg/(m.s)

| v_t | Terminal settling velocity | 0.2184 m/s |

3 Results and discussions

The results in the present study are structured in the following way. First, the development of the three different anisotropic drag closures with different levels of complexity (one marker, two markers and 3 markers) are presented. The 2-marker closure, which has previously appeared in a peer-reviewed publication (Cloete et al., 2018a), is only discussed briefly for context, whereas the newly derived 1-marker and 3-marker closures are discussed in more detail. Second, the closures are evaluated in an *a priori* manner by comparing observations from the resolved periodic TFM simulations to model predictions. Third, the closures are evaluated in an *a posteriori* manner by comparing the results of resolved TFM simulations to those of coarse-grid fTFM simulations over a range of fluidization conditions.

3.1 Closure development

In a previous study (Cloete et al., 2018a), it was shown that accurate anisotropic filtered drag force closures can be constructed based on the drift velocity approach (Ozel et al., 2013; Parmentier et al., 2012), as shown in Equation 11.

$$\overline{K_{gs}(v_{g,\iota} - v_{s,\iota})} = C_{NL} K_{gs,hom}(\tilde{v}_{g,i} - \tilde{v}_{s,i} - v_{d,i})$$

Equation 8

Contrary to previous studies based on the drift velocity approach (Ozel et al., 2013; Ozel et al., 2017; Parmentier et al., 2012; Schneiderbauer and Saeedipour, 2018) it was found that a closure for the non-linearity correction factor, C_{NL}, is necessary for industrially relevant filter sizes. The reason for this different conclusion is that the previous work on the drift velocity approach were all based on 3D fine-grid simulations that were limited to small domain sizes, and therefore small filter sizes, due to the computational cost of 3D simulations. However, it was previously shown from both 2D and 3D data (Cloete et al., 2018a) that the importance of the non-linearity correction factor increases substantially with increasing filter size. It can increase the modelled filtered drag force by up to a factor of 2 at grid sizes relevant to industrial scale simulations (Cloete et al., 2018a), and should therefore be closed.

It was found that this non-linearity correction factor, which accounts for assumptions when deriving the drift-velocity form of the filtered drag force, can be accurately closed using an isotropic 2-marker closure. Furthermore, the benefit of such a closure was demonstrated in 2D verification cases, where it reduced the grid dependence in coarse-grid simulations of bubbling fluidization. This closure from our earlier study (Cloete et al., 2018a) is deemed sufficient for the present study, which will focus on the closure for the drift velocity. We note in passing that the closure for $v_{d,i}$ has a substantially larger effect on the filtered drag force than that for C_{NL} (Cloete et al., 2018a), motivating our argument.

3.1.1 2-marker closure

First, a description of the anisotropic 2-marker closure presented in our previous study (Cloete et al., 2018a) is briefly repeated here in Equation 12 to Equation 15, since the other two closures that will be discussed in the present study are based on this 2-marker closure. It can be noted that, in the present study, the slip velocity is defined as the difference between the gas and solid phase velocities ($v_{g,i} - v_{s,i}$), whereas the filtered slip velocity is the difference between the filtered values ($\tilde{v}_{g,i} - \tilde{v}_{s,i}$). Finally, the adjusted slip velocity, to which the modelled filtered drag force is proportional to, is defined as the difference between the filtered slip velocity and the drift velocity ($\tilde{v}_{g,i} - \tilde{v}_{s,i} - v_{d,i}$). In the closures, the filtered slip velocity, drift velocity and adjusted slip velocity are all scaled based on the steady state

sedimentation speed of the suspension evaluated at the filtered solids volume fraction. This is motivated by previous work that found that such an approach results in a simpler dependency of the closure on the filtered solids volume fraction (Cloete et al., 2018a).

In Equation 12 to Equation 15 it can be seen that the drift velocity was found to consist of two contributions: one that acts only in the direction aligned with gravity and which is independent of the filtered slip velocity, i.e., the term k_1 in Equation 13, and another that is proportional to the filtered slip velocity in the direction considered, i.e., the term $\tilde{v}_{slip,i}^*(1 - 10^{-k_2})$ in Equation 13. In the latter contribution, a larger value of k_2 means that the drift velocity contribution will be a larger proportion of the filtered slip velocity, which results in a smaller adjusted slip velocity in Equation 12. Additionally, it was found that k_2 increases with increasing absolute values of the filtered slip velocity in the direction considered. This is in agreement with earlier isotropic 2-marker models (Gao et al., 2018; Milioli et al., 2013; Sarkar et al., 2016; Schneiderbauer and Pirker, 2014) that generally found the drag correction to increase with increasing filtered slip velocity magnitude.

$$v_{adj,i}^* = \tilde{v}_{slip,i}^* - v_{d,i}^* \qquad\qquad\text{Equation 9}$$

$$v_{d,i}^* = k_1 + \tilde{v}_{slip,i}^*(1 - 10^{-k_2}) \qquad\qquad\text{Equation 10}$$

$$k_1 = x_1\left(\frac{2}{\pi}\right)(\overline{\alpha_s}^{x_2})\,\text{atan}\left(x_3 \max(x_4 - \overline{\alpha_s}, 0)\right) \qquad\qquad\text{Equation 11}$$

$k_1 = 0$ if i is in the direction perpendicular to gravity

$$k_2 = \left(\frac{2}{\pi}\right)^2 \text{atan}(x_5\overline{\alpha_s})\,\text{atan}\left(x_3 \max(x_4 - \overline{\alpha_s}, 0)\right)\left(x_6\overline{\alpha_s}^{x_7}\right.$$
$$\left. + x_8\left(\frac{2}{\pi}\right)\text{atan}\left(x_9\overline{\alpha_s}^{x_{10}}|\tilde{v}_{slip,i}^*|\right)\log|\tilde{v}_{slip,i}^*|\right) \qquad\qquad\text{Equation 12}$$

$x_1 = -1.40$, $x_2 = 1.38$, $x_3 = 48.5\left(\frac{2}{\pi}\right)\text{atan}\left(0.235\Delta_{fil}^*\right)$, $x_4 = 0.553$, $x_5 = 333\Delta_{fil}^*{}^{1.92}$,

$x_6 = 1.76\left(\frac{2}{\pi}\right)\text{atan}\left(1.29\Delta_{fil}^*\right)$, $x_7 = 1/(2.40\Delta_{fil}^*{}^{0.234})$, $x_8 = 1/\left(2.44\left(\frac{2}{\pi}\right)\text{atan}\left(1.92\Delta_{fil}^*\right)\right)$,

$x_9 = 25.6\Delta_{fil}^*$ and $x_{10} = 1.56$.

It is noted that the filter size is non-dimensionalized as $\hat{\Delta}_f = \Delta_f / (\frac{v_t}{g^2})$, as commonly done in the fTFM literature (Igci et al., 2008; Milioli et al., 2013; Sarkar et al., 2016). Furthermore, in the closures, a re-scaled filter size is defined as $\Delta_f^* = \max(\hat{\Delta}_f - \hat{\Delta}_{f,\min}, 0)$. $\hat{\Delta}_{f,\min}$ is set to 0.1285, the dimensionless grid size at which the fine grid simulations were performed. The use of this re-scaled filter size in the closures ensures that the fTFM closures tend to no sub-grid corrections when the filter size tends to the grid size used in the resolved TFM simulations (Cloete et al., 2018b).

The gravitational contribution, k_1 in Equation 11, warrants further discussion, since it forms an integral part of all three anisotropic closures presented in our present study. This contribution means that, when considering the gravity aligned direction, a positive (i.e., vertically upward) filtered drag force will be predicted for a filtered slip velocity of zero. A possible explanation for this interesting phenomenon is that instances of negative slip velocity (i.e., vertically downward) are most likely to occur in regions of low particle concentration where the gas flow can respond rapidly to short-lived negative forces arising from dynamic pressure fluctuations in the bed. Since the drag force increases super-linearly with the solids volume fraction in a homogeneous suspension, the following scenario will then give a positive (i.e., upward) total drag force in the filter region at zero filtered slip velocity: a

positive force resulting from a positive slip in a dense region will outweigh the relatively small negative force created by negative slip velocities in dilute regions. In such a scenario, the filtered vertical gas and solids velocities may cancel each other out (leading to a zero filtered slip velocity), but still result in a positive vertical filtered drag force. The likelihood of this situation occurring will increase with filter size and filtered solids volume fraction (up to a certain packing where the suspension becomes homogenous), since both these factors will increase the probability of both dilute and dense regions occurring in a filter region.

It should be noted that the instances of near-zero filtered slip velocities discussed here represent only a small fraction of the total samples in the fine-grid data. Also, the time-averaged filtered slip velocity will still tend to be directed upwards, therefore the speculation about occasional negative slip velocities does not contradict the well-established fact that the gas will tend to rise faster in dilute regions than in dense emulsions.

The expected trends of a larger gravitational contribution with an increase in filter size and filtered solids volume fraction were clearly observed in the data from fine-grid simulations presented in our previous study (Cloete et al., 2018a), and are reflected in the closure in Equation 14. A further consequence of the gravitational contribution is that, at small positive filtered slip velocities in the vertical direction, the predicted filtered drag force is in fact greater than the drag force predicted by the microscopic drag force evaluated at the filtered values. This behaviour corresponds to the data from our fine-grid simulations, and was also recently observed by Schneiderbauer and Saeedipour (2018) in 3D resolved TFM simulations. The isotropic fTFM drag closures common in literature do not account for this effect (which is prominent at small filtered slip velocities and large filter sizes), since they assume that the filtered drag force is always smaller than the microscopic drag force evaluated at the filtered values.

It should be noted that the way that the anisotropy is accounted for in the 2-marker closure, as well as in the other anisotropic closures presented subsequently, does not satisfy Galilean invariance, specifically rotational invariance. However, the proposed closures will remain reasonable as long as a Cartesian or 2D axisymmetric coordinate system is used with the vertical axis aligned with gravity. Since the vast majority of fluidized simulations will meet this requirement, the lack of rotational invariance should not be a significant limitation in practice. The positive results in the remainder of the present study also indicate that the approach to account for anisotropy is sufficient, especially when considering that the purpose of the fTFM is to serve as a pragmatic modelling tool to enable reasonably accurate simulations of industrial-scale fluidized beds. It can, however, be noted that a methodology for constructing Galilean invariant anisotropic drag closures was recently discussed by Jiang et al. (2018), although these authors did not attempt to establish such a closure. Since the anisotropic closures proposed in the present study appear to perform satisfactorily, the derivation of Galilean invariant closures will also not be attempted here but is recommended for future work.

3.1.2   1-marker closure

Next, a simplified 1-marker closure, Equation 16 to Equation 19, is constructed to evaluate the importance of the filtered slip velocity as marker in the 2-marker closure. This is done by neglecting the filtered slip velocity as an independent variable in the expression for k_2 in Equation 19, therefore the drift velocity contribution proportional to the filtered slip velocity no longer increases with increasing filtered slip velocity.

$$v_{adj,i}^* = \tilde{v}_{slip,i}^* - v_{d,i}^* \qquad\qquad \textit{Equation 13}$$

$$v_{d,i}^* = k_1 + \tilde{v}_{slip,i}^*(1 - 10^{-k_2}) \qquad\qquad \textit{Equation 14}$$

$$k_1 = x_1 \left(\frac{2}{\pi}\right) (\overline{\alpha_s}^{-x_2}) \operatorname{atan}\left(x_3 \max(x_4 - \overline{\alpha_s}, 0)\right)$$

$k_1 = 0$ if i is in the direction perpendicular to gravity

$$k_2 = \left(\frac{2}{\pi}\right)^2 \operatorname{atan}(x_5 \overline{\alpha_s}) \operatorname{atan}\left(x_3 \max(x_4 - \overline{\alpha_s}, 0)\right)(x_6 \overline{\alpha_s}^{-x_7})$$

$x_1 = -3.44$, $x_2 = 2.09$, $x_3 = 21.6 \left(\frac{2}{\pi}\right) \operatorname{atan}(0.216\Delta_{fil}^*)$, $x_4 = 0.559$, $x_5 = 99.7\Delta_{fil}^{*\,3.31}$, $x_6 = 2.19$ and $x_7 = 1/(2.08\Delta_{fil}^{*\,0.246})$.

Using the coefficients above, a fit with $R^2 = 0.990$ is obtained against the binned data. Since the filtered slip velocity is not used as a marker in the binning procedure, the mean filtered slip velocity in each filtered solids volume fraction bin is used in Equation 17 when calibrating the parameters of the closure model. Since each bin does not have a fixed filtered slip velocity value, the binned data for the 1-marker model is best displayed in the form $-\log(1 - v_{d,i}^*/\tilde{v}_{slip,i}^*)$, as shown in Figure 2. From the binned data, it is clear that this scaled ratio of the drift velocity to the filtered slip velocity is dependent on the direction considered. Importantly, it can be seen that the 1-marker model proposed in this section accurately predicts the binned data in both directions due to the anisotropic contribution in Equation 18. Furthermore, the drift velocity correctly goes to zero in the limits of dilute and dense filtered solids volume fractions.
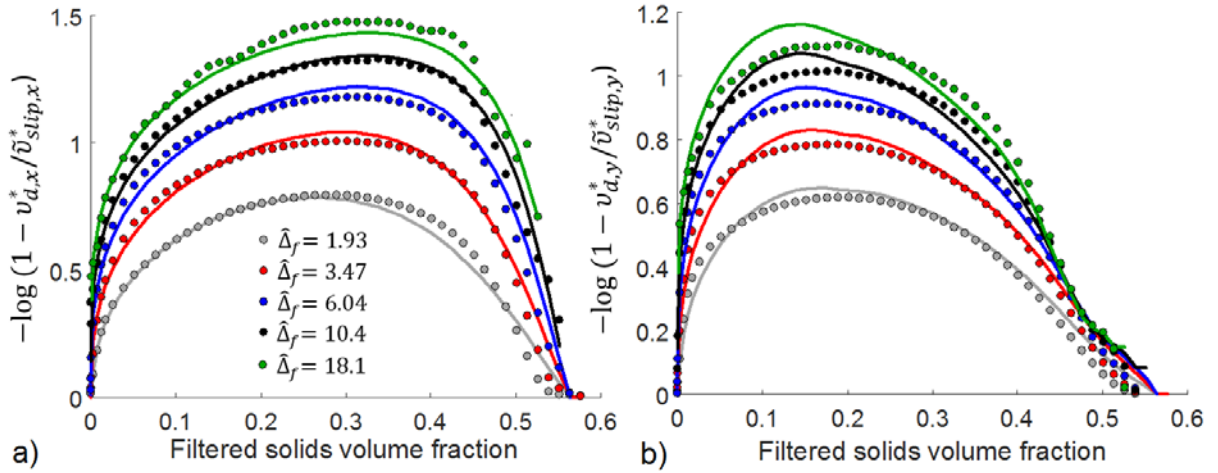

Figure 2 – The average value of $-\log(1 - v_{d,i}^*/\tilde{v}_{slip,i}^*)$ plotted against the filtered solids volume fraction for a) the lateral direction and b) the vertical direction. Symbols show the binned observations and lines the closure model predictions.

3.1.3 3-marker closure

While investigating anisotropic closures for the meso-scale solids stresses (Cloete et al., 2018b), it was found that a filtered co-variance quantity in the form of $\overline{X'Y'}$ can be modelled by a marker of the form $M = \left(\frac{d\bar{X}}{dx}\frac{d\bar{Y}}{dx} + \frac{d\bar{X}}{dy}\frac{d\bar{Y}}{dy}\right)$, referred to as the "gradient product marker" (GPM). This approach can similarly be applied to the drift velocity, when it is redefined as follows: $v_{d,i} = \frac{\overline{\alpha'_g v'_{g,\iota}}}{\bar{\alpha}_s \bar{\alpha}_g}$. The derivation of this definition is given in the appendix. Applying the GPM concept to the scaled drift velocity, the "drift GPM" can be expected to be a promising candidate as a third marker in the drift velocity closure. It can be defined in 2D as follows:

$$\mathrm{M}_{drift,i} = \frac{\left(\frac{d\overline{\alpha_g}}{dx}\frac{d\overline{v_{g,\iota}}}{dx} + \frac{d\overline{\alpha_g}}{dy}\frac{d\overline{v_{g,\iota}}}{dy}\right)}{\overline{\alpha_s}\,\overline{\alpha_g}\,\overline{v}_{ss\_slip}} \qquad \text{Equation 17}$$

Note, that we use $\overline{v_{g,\iota}}$ here, i.e., the algebraic average gas-phase velocity, and not the Favre-average velocity $\tilde{v}_{g,i}$. Additionally, $\bar{v}_{ss\_slip}$ refers to the steady state sedimentation velocity evaluated at the filtered solids volume fraction.

In the present study, the drift GPM is non-dimensionalized as $\widehat{\mathrm{M}}_{drift,i} = \mathrm{M}_{drift,i}\,\frac{v_t^4}{g^2}$. Additionally, since the GPM is highly dependent on the filter size, the following scaling is applied for the binning process to ensure a better distribution of data through the parameter space:

$$M^*_{drift,i} = \frac{\widehat{\mathrm{M}}_{drift,i}}{a\Delta_f^{*\,(b+c\Delta_f^*)}} \qquad \text{Equation 18}$$

Where $a = 3.28$, $b = -1.81$ and $c = -0.0120$. $M^*_{drift,i}$ will henceforth be referred to as the scaled drift GPM.

For the 3-marker closure proposed in this section, the adjusted slip velocity is binned for each filter size as a function of the filtered solids volume fraction, the scaled filtered slip velocity in the direction considered and the scaled drift GPM in the direction considered. The binned data for the scaled adjusted slip velocity is shown in Figure 3 plotted against the scaled drift GPM. It is clear that there is a strong dependence of the adjusted slip velocity with respect to the drift GPM at both small and large filter sizes. The drift GPM dependence appears to be of similar importance as the filtered slip velocity dependence.

Specifically, increasing drift GPM values lead to smaller adjusted slip velocities, and therefore also smaller filtered drag forces. At the smaller filter size considered, the scaled adjusted slip velocity tends to flatten out at large absolute values of the drift GPM. At the larger filter size considered, such a trend cannot be clearly distinguished. However, this is most likely due to the fact that large enough GPMs do not occur in the resolved simulations: intermediate filter sizes, for which the results are not shown here, confirm that the adjusted slip velocity becomes independent of the drift GPM at large absolute values of the drift GPM. Lastly, it is noted that there appears to be some correlation between the filtered slip velocity and the drift GPM for a specific direction. As seen from Figure 3, the drift GPM tends to be positive at large positive slip velocities and negative at large negative slip velocities.
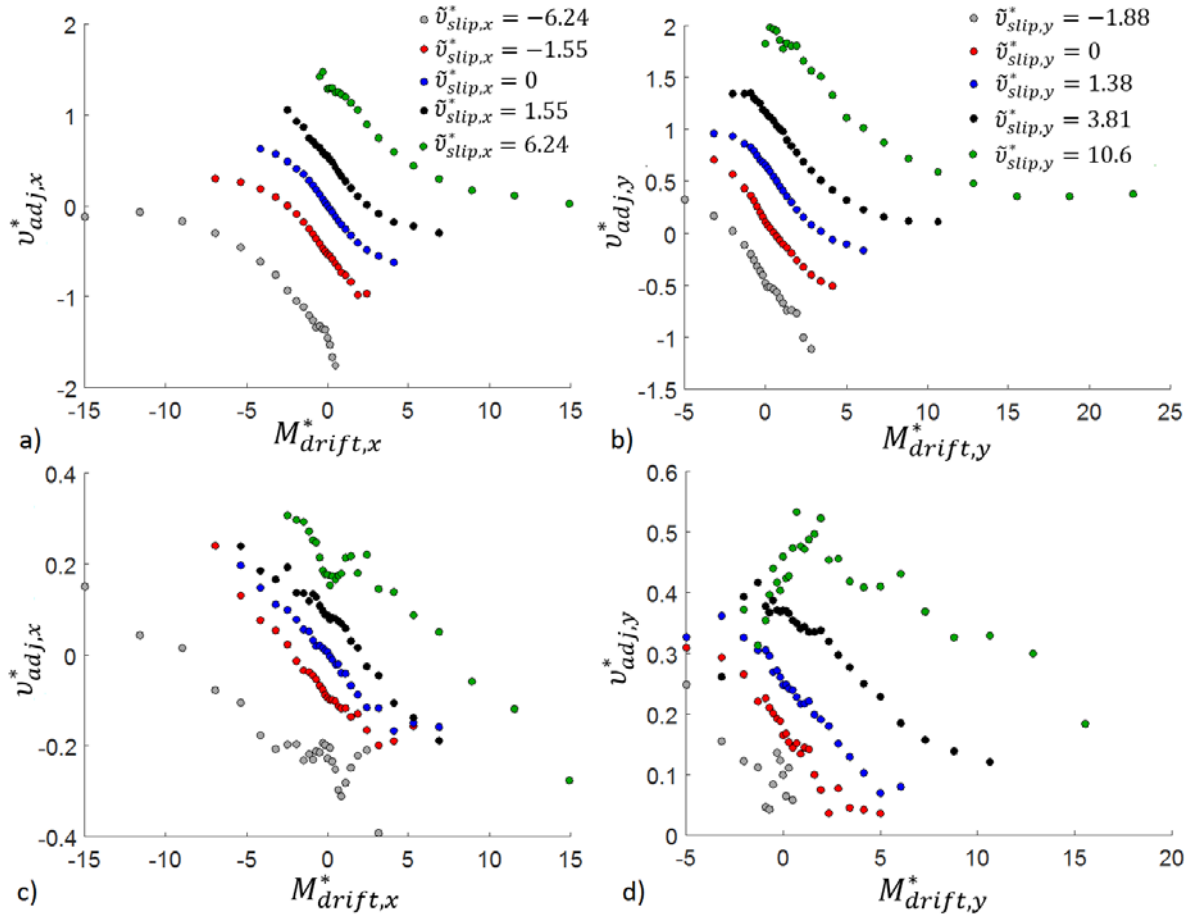
Figure 3 - The scaled adjusted slip velocity for the lateral direction (left) and vertical direction (right) plotted against the scaled drift GPM at $\hat{\Delta}_f = 1.93$ (top) and $\hat{\Delta}_f = 18.1$ (bottom). The data shown is for an intermediate filtered solids volume fraction, $\overline{\alpha_s} = 0.251$.

It is interesting to note the similarities between the proposed drift GPM and the theory-based closures of Schneiderbauer (2017). Firstly, the latter study found that the sub-grid drag reduction increased with increasing solids volume fraction variance, which was found to be proportional to the magnitude of the gradient of the filtered solids volume fraction. Secondly, Schneiderbauer (2017) found that the sub-grid drag correction also increased with increasing sub-grid gas-phase stresses, which was found to be proportional to the gas-phase shear rate magnitude (i.e., the filtered gas phase velocity gradients). Similarly, in the present study, we find that the sub-grid drag correction increases with increasing values of the drift GPM, which is proportional to the gas volume fraction and velocity gradients. However, an important difference is that the present study does not account for the production of sub-grid stresses due to interfacial work, as described by Schneiderbauer (2017). On the other hand, the drift GPM allows for a decrease in the sub-grid drag reduction in case the filtered gas volume fraction gradients and gas velocity gradients are not correlated (i.e., have different signs). This aspect is not included in the theory of Schneiderbauer (2017). Future work is therefore suggested to explore the similarities and differences of these two approaches.

Through a rigorous analysis of the binned data, it was found that the scaled adjusted slip velocity could be closed using the 3-marker closure given by Equation 22 to Equation 26 and the set of coefficients summarized below Equation 26. The third marker adds a substantial amount of complexity to the closure fitting process. This is due to (i) the large increase in the number of bins caused by the added dimension in the binned data, and (ii) due to the complex interactions between the different markers.

The process that was used to overcome this complexity is described in greater detail in the thesis of Cloete (2018) for the interested reader.

Compared to the 2-marker model, it can be seen that the gravitational and slip velocity contributions (i.e., k_1 and $\tilde{v}_{slip,i}^*(1 - 10^{-k_2})$, respectively) remain similar, with only minor changes in the filter size dependencies of the coefficients. Most important, it is found that the effect of the drift GPM can be included as an additional term k_3, which is denoted as the "gradient contribution term" in what follows. Therefore, gradients in the flow (specifically in the filtered gas volume fraction and in the algebraically averaged gas velocity field) can be identified as an additional source of drift velocity. It can be physically understood that large drift GPMs in a coarse grid filtered simulation indicates the presence of a cluster interface, which cannot be well resolved on a coarse grid. It is well known that poor cluster interface resolution overpredicts gas-solid contact, leading to overpredictions of interphase mass, momentum and energy transfer. The use of the drift GPM as marker allows the model to directly address this overprediction of momentum transfer.

In the gradient contribution term, i.e., k_3 in Equation 26, the first two arctangent functions ensure that the gradient contribution to the drift velocity is zero at the dilute and dense limits. The third arctangent function, i.e., $atan(x_{13}\widehat{M}_{drift,i})$, causes the gradient contribution to saturate at large absolute values of the drift GPM, as observed in the binned data. The filter size dependency of x_{13} compensates for the fact that the dimensionless drift GPM decreases rapidly with increasing filter size. Therefore, at large filter sizes, the gradient contribution saturates at smaller drift GPM values.

The next three terms identify different parts of the gradient contribution. The first part (proportional to x_{14}) is due to only the drift GPM and takes the sign of the drift GPM. The second part (proportional to $\left(x_{16}\left|\overline{\alpha}_s - \frac{x_4}{2}\right|^{x_{17}} + x_{18}\right)$) is due to the interaction of the drift GPM and the filtered slip velocity, since it is observed that the gradient contribution increases at large absolute slip velocities. It is found that this part has a minimum effect at intermediate volume fractions, but the effect increases towards the dilute and dense limits. However, it can be noted that the first two arctangent functions still ensure that this part goes to zero at the dilute and dense limits. Furthermore, this GPM-slip interaction part of the gradient contribution takes the sign of the drift GPM and its absolute value is symmetrical around a drift GPM of zero.

The third part of the gradient contribution (proportional to x_{19}) is an asymmetrical GPM-slip interaction part, since it is observed that, near the dilute and dense limits, there is an additional effect in case the drift GPM and the filtered slip velocity have opposite signs. This asymmetrical effect can clearly be seen in Figure 4, where the drift GPM dependence is compared at dilute and intermediate volume fractions. The asymmetrical GPM-slip interaction part has no effect at intermediate volume fractions, but the effect increases towards the dilute and dense limits, similarly to the symmetrical GPM-slip interaction part. In the closure model, by using $\min(sign(\tilde{v}_{slip,i}^*\widehat{M}_{drift,i}), 0)$, this part is defined in such a way that it only has an effect in case the drift GPM and the filtered slip velocity has opposite signs. Also, this part has the opposite sign as the drift GPM. The asymmetrical interaction part therefore has an effect in the opposite direction as the symmetrical interaction part.

$$v_{adj,i}^* = \tilde{v}_{slip,i}^* - v_{d,i}^* \qquad\qquad \textit{Equation 19}$$

$$v_{d,i}^* = k_1 + \tilde{v}_{slip,i}^*(1 - 10^{-k_2}) + k_3 \qquad\qquad \textit{Equation 20}$$

$$k_1 = x_1\left(\frac{2}{\pi}\right)(\overline{\alpha}_s^{x_2})\,atan\left(x_3 \max(x_4 - \overline{\alpha}_s, 0)\right) \qquad\qquad \textit{Equation 21}$$

$k_1 = 0$ if i is in the direction perpendicular to gravity

$$k_2 = \left(\frac{2}{\pi}\right)^2 \operatorname{atan}(x_5\overline{\alpha_s}) \operatorname{atan}\left(x_3 \max(x_4 - \overline{\alpha_s}, 0)\right)\left(x_6\overline{\alpha_s}^{x_7}\right.$$
$$\left. + x_8\left(\frac{2}{\pi}\right) \operatorname{atan}\left(x_9\overline{\alpha_s}^{x_{10}}|\tilde{v}_{slip,i}^*|\right) log|\tilde{v}_{slip,i}^*|\right)$$

Equation 22

$$k_3 = \left(\frac{2}{\pi}\right)^3 \operatorname{atan}(x_{11}\overline{\alpha_s}) \operatorname{atan}\left(x_{12} \max(x_4 - \overline{\alpha_s}, 0)\right) atan\left(x_{13}\widehat{M}_{drift,i}\right)\left\{x_{14}\right.$$
$$+ |\tilde{v}_{slip,i}^*|^{x_{15}}\left[\left(x_{16}\left|\overline{\alpha_s} - \frac{x_4}{2}\right|^{x_{17}} + x_{18}\right)\right.$$
$$\left.\left. + \min\left(sign\left(\tilde{v}_{slip,i}^*\widehat{M}_{drift,i}\right), 0\right) x_{19}\left|\overline{\alpha_s} - \frac{x_4}{2}\right|^{x_{17}}\right]\right\}$$

Equation 23

$x_1 = -1.74\left(\frac{2}{\pi}\right) atan\left(1.71\Delta_{fil}^*\right),\ x_2 = 1.54,\ x_3 = 21.8\left(\frac{2}{\pi}\right) atan\left(0.708\Delta_{fil}^*\right),\ x_4 = 0.558,$

$x_5 = 45.6\Delta_{fil}^{*\,2.10},\ x_6 = 2.09\left(\frac{2}{\pi}\right) atan\left(0.331\Delta_{fil}^*\right),\ x_7 = 0.248,\ x_8 = 0.308\,,\ x_9 = 6.35\Delta_{fil}^*,$

$x_{10} = 1.22,\ x_{11} = 4030,\ x_{12} = 194,\ x_{13} = 0.0742\Delta_{fil}^{*\,1.89},\ x_{14} = 1/\left(3.53\left(\frac{2}{\pi}\right) atan\left(0.303\Delta_{fil}^*\right)\right),$

$x_{15} = 1/\left(1 + 4.69\left(\frac{2}{\pi}\right) atan\left(0.0604\Delta_{fil}^*\right)\right),\ x_{16} = 9.18,\ x_{17} = 2.84,\ x_{18} = 1/\left(2.24\Delta_{fil}^*\right)$ and

$x_{19} = 1/\left(0.0742\left(\frac{2}{\pi}\right) atan\left(0.419\Delta_{fil}^*\right)\right).$

The closure model presented in this section yields an excellent fit to the binned data over all filter sizes with $R^2 = 0.979$. This is demonstrated for the intermediate filter size in Figure 5, where the scaled adjusted slip velocity is plotted against the filtered solids volume fraction at different filtered slip velocities and scaled drift GPM values. Additionally, Figure 4 shows how the closure models capture the drift GPM dependency to predict the scaled adjusted slip velocity.
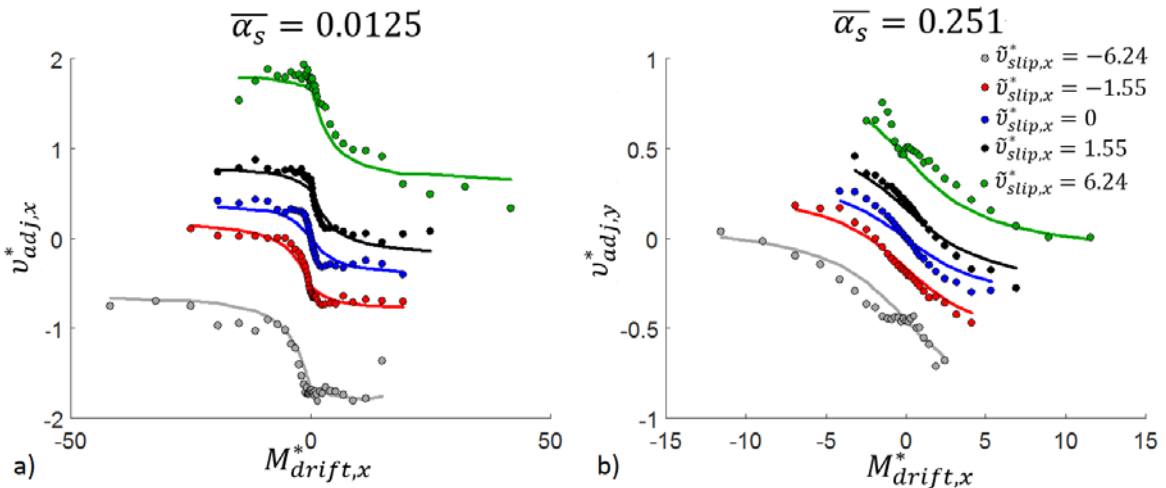

Figure 4 - The scaled adjusted slip velocity for the lateral direction plotted against the scaled drift GPM at $\widehat{\Delta}_f = 5.91$ for a) a dilute filtered solids volume fraction, $\overline{\alpha_s} = 0.0125$ and b) an intermediate filtered solids volume fraction, $\overline{\alpha_s} = 0.251$.
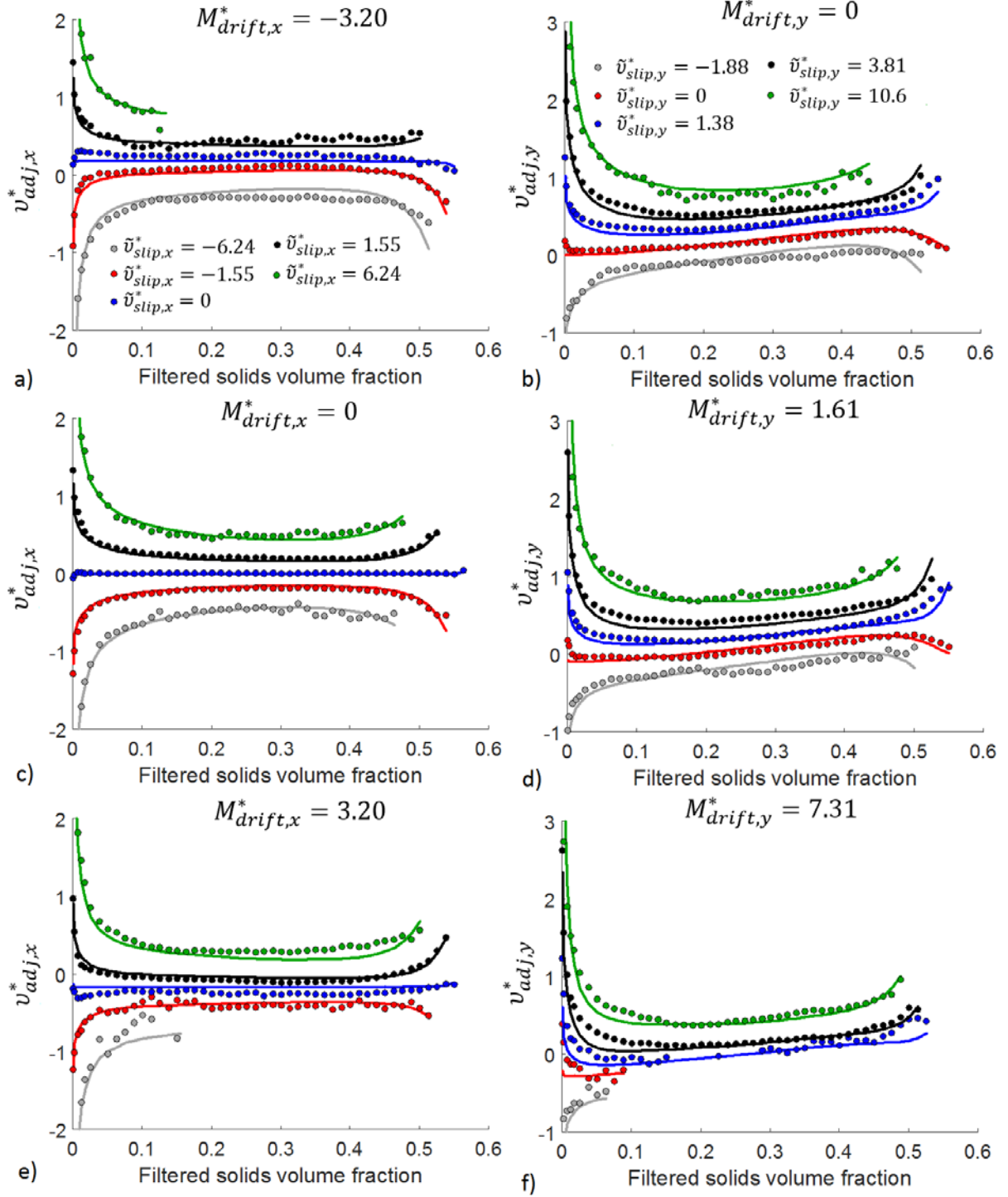
Figure 5 - The scaled adjusted slip velocity for the lateral direction (left) and the vertical direction (right) plotted against the filtered solids volume fraction at $\hat{\Delta}_f = 5.91$ for different scaled drift GPMs (top, centre and bottom rows).

A potential issue with using the drift GPM is that, as can be noted from Equation 20, the definition of the drift GPM requires the algebraic average of the gas velocities in the filter region. However, the filtered momentum transport equations, discussed in section 2.2, solves for the phase-weighted gas velocities. From the derivation of the newly proposed drift velocity definition (see the appendix) it is found that the algebraic average of the gas velocity can be calculated as:

$$\overline{v_{g,\iota}} = \tilde{v}_{g,i} - \bar{\alpha}_s v_{d,i}$$

It is therefore clear that the model prediction for the drift velocity (which requires the drift GPM to be known) is required to calculate $\overline{v_{g,\iota}}$, which is necessary to calculate the drift GPM. Thus, the algebraic average of the gas velocity is implicitly defined. Fortunately, this can easily be solved via a simple iteration loop: For the current iteration, the value of the drift velocity from the previous iteration is used to calculate $\overline{v_{g,\iota}}$, the drift GPM, the new drift velocity and the filtered drag force, in that order. For the first iteration of the simulation the $\overline{v_{g,\iota}}$ can simply be approximated as $\tilde{v}_{g,i}$ to calculate the drift GPM.

Furthermore, two additional factors ensure that this process is robust. Firstly, as shown in Table 3, $\overline{v_{g,\iota}}$ is highly correlated with $\tilde{v}_{g,i}$, even at large filter sizes. Therefore, a very good approximation of the drift GPM could be obtained even if $\tilde{v}_{g,i}$ was used in Equation 20. Secondly, because of the very strong correlation between the drift velocity and the filtered slip velocity, the drift velocity can be predicted to a high degree of precision using the 3-marker closure model derived later in this section. This is in contrast to the adjusted slip velocity, which is much more difficult to predict precisely, as will be shown in section 3.2. It can also be seen that the correlation between observed values and model predictions for the drift velocity increases at large filter sizes, when the correlation between the drift velocity and the filtered slip velocity is even stronger. As a result of these two factors and the iterative procedure followed, the estimate of $\overline{v_{g,\iota}}$ used to calculate the drift GPM will always be very accurate.

Table 3 – Coefficient of determination (R^2) for the correlation of $\overline{v}_{g,i}$ and $\tilde{v}_{g,i}$ as observed in the resolved simulations, as well as for the correlation between observed values and model predictions (using the 3-marker closure) for the drift velocity, $v_{d,i}$. Results are shown for two filter sizes.

$\hat{\Delta}_f$	Correlation between $\overline{v}_{g,i}$ and $\tilde{v}_{g,i}$		Correlation between observed and predicted values for $v_{d,i}$	
	Lateral direction	Vertical direction	Lateral direction	Vertical direction
1.93	0.9991	0.9990	0.8481	0.8712
18.1	0.9973	0.9931	0.9865	0.9920

3.2   *A priori* analysis

The three filtered drag force closures that were proposed in section 3.1 are evaluated in this section by comparing the model predictions based on these closures to the observed values in the periodic resolved fTFM simulations used to derive the closures. A larger value of the coefficient of determination, R^2, means that the closure explains more of the variance in the data directly and less of the variance is averaged out during the binning process. It can therefore be expected that a closure that can achieve a higher R^2 in such an *a priori* analysis should also perform better in coarse grid simulations that are significantly different from the conditions under which the closures were derived. It can be noted that an R^2 value of 1 means a perfect correlation between observed and modelled values, whereas a value of 0 corresponds to replacing the model predictions with the mean of the observed values.

Figure 6 summarises the results when comparing the observations and predictions for samples in the resolved simulation data as a function of the dimensionless filter size. It can be noted that the grid sizes used in the *a posteriori* analyses in section 3.3 correspond to dimensionless filter sizes of $\hat{\Delta}_f = 2.06$ (10 mm grid cells), $\hat{\Delta}_f = 4.12$ (20 mm grid cells) and $\hat{\Delta}_f = 8.23$ (40 mm grid cells), respectively,

assuming that the filter size is set equal to the grid size. Results are shown for the 1-marker, 2-marker and 3-marker closures presented in this study. Additionally, an isotropic 2-marker closure (Cloete et al., 2018a) is also included for perspective. It was previously reported (Cloete et al., 2018a) that, as can be seen in Figure 6, such an isotropic closure completely fails in the lateral direction and also performs worse than the anisotropic 2-marker closure in the vertical direction.

Regarding the anisotropic closures, it is observed that the model predictions are significantly improved as the number of markers in the anisotropic closure is increased. In the lateral direction, there is a substantial improvement at all filter sizes when increasing from 2 to 3 markers, whereas the improvement when going from 1 to 2 markers reduces at large filter sizes. For the vertical direction, the improvement with increasing number of markers generally reduces at large filter sizes. It is interesting to note that the simple 1-marker anisotropic closure outperforms the 2-marker isotropic closure even in the vertical direction. Considering that the vertical direction data was used to derive the isotropic closure, this result provides clear evidence to the benefits of closing the filtered drag force based on the drift velocity formulation (while also considering an anisotropic gravitational contribution to the drift velocity).
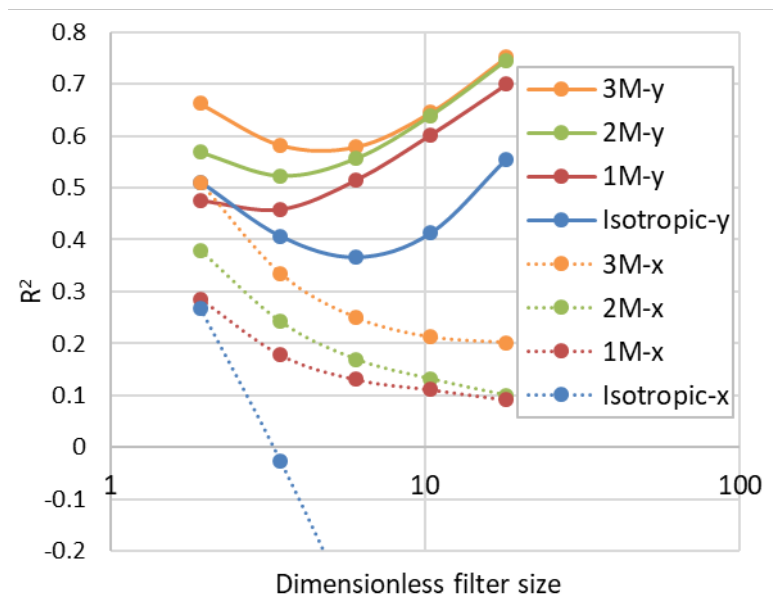

Figure 6 – The coefficient of determination as a function of the dimensionless filter size for the lateral and vertical direction and for four different closures developed for the filtered drag force.

It was previously argued (Cloete et al., 2018a) that the gravitational contribution to the drift velocity appears relatively easy to model. This explains the substantially higher R^2 values in the vertical direction, where a mean positive filtered drag force contribution is observed, compared to the lateral direction, where no such mean contribution is present. In the lateral direction, positive and negative filtered drag forces will tend to cancel out each other at large filter sizes. This results in generally small filtered drag forces with limited variance in the sample data. Consequently, model deviations of a similar magnitude to those in the y-direction will result in small R^2-values. The hypothesis about the gravitational contribution also offers an explanation for the increasing R^2 values with increasing filter size in the vertical direction when larger filter sizes are considered, since the relative magnitude of the gravitational contribution increases at large filter sizes (Cloete et al., 2018a).

Finally, the gravitational contribution can also help to explain the trend in Figure 6 that increasing the number of markers does not improve the predictions in the vertical direction when large filter sizes are considered. This is because the closure for the gravitational contribution is only a function of the

filter size and the filtered solids volume fraction (see Equation 14, Equation 18 and Equation 24) and its relative importance increases with increasing filter size. Increasing the number of markers in the closure therefore does not improve the prediction of the gravitational contribution, which is dominant in the vertical direction at large filter sizes. This is especially evident when going from 2 to 3 markers, since the flow gradients tend to be small at the largest filter sizes, resulting in a negligible effect of the drift GPM as a marker compared to the gravitational contribution. However, in the lateral direction, where no gravitational contribution is present, the drift GPM in the 3-marker closure still has a significant positive effect at larger filter sizes, considering the generally small filtered drag forces in the lateral direction, as described earlier.

In conclusion, it can be noted that the predictive capability of the anisotropic closures significantly increases with increasing markers considered, with the 3-marker model also offering a clear improvement compared to the simpler anisotropic closures, especially at smaller filter sizes. However, from section 3.1.3, it is also clear that including the gradient contribution to the adjusted slip velocity closure substantially complicates the derivation process, as well as the resulting closure expression. The verification exercises in section 3.3 will therefore further evaluate whether the more complex 3-marker drag closure results in any practical improvements in coarse grid simulations.

3.3 *A posteriori* analysis

This section will assess the performance of the anisotropic filtered drag force closures at different levels of complexity based on their performance in coarse grid simulations of bubbling, turbulent and core-annular fluidization. Again, and for perspective, an isotropic 2-marker closure is also evaluated, since an earlier study (Cloete et al., 2018a) compared the 2-marker isotropic and anisotropic closures only for bubbling fluidization.

It can be noted that the filter-to-grid-size ratio employed in the closures was optimised for each combination of fTFM closures investigated to predict the bed expansion to within 2% of the resolved TFM prediction for the bubbling case and on the 10 mm grid. All the other simulations for a specific closure combination were then run with the same filter-to-grid-size ratio to evaluate the grid dependency and the generality of the closures. A summary of the different cases and the filter-to-grid-size ratios used for each case is shown in Table 4. A case with no fTFM closures was included for each of the three fluidization regimes considered to illustrate the importance of fTFM closures.

Table 4 – A summary of the combinations of closures considered in the verification study, as well as the filter/grid ratio that was determined to be optimal for each case on the 10 mm grid.

Case	Adjusted slip velocity	Non-linearity correction factor	Meso-scale interphase force	Filter/grid ratio
1	Anisotropic 2-marker	Isotropic 2-marker	Anisotropic 2-marker	1.0
2	None	None	None	Not applicable
3	As part of an isotropic drag correction factor			1.9
4	Anisotropic 1-marker	Isotropic 2-marker	Anisotropic 2-marker	1.0
5	Anisotropic 3-marker	Isotropic 2-marker	Anisotropic 2-marker	1.8

The approach of specifying different filter-to-grid-size ratios for different closures is justified based on our finding that the optimal filter-to-grid-size ratio in coarse-grid simulations is significantly influenced by the closure formulation and the choice of markers. Using a single filter-to-grid-size ratio for all cases would therefore arbitrarily disadvantage some closures, while favouring others. To ensure a fair comparison, the optimal filter-to-grid-size ratio is determined for each closure and the performance of a specific closure is evaluated based on its grid-independence and generality when using this optimal filter-to-grid-size ratio. As an example, the isotropic drag closure requires a larger filter-to-grid-size ratio to compensate for overpredicted lateral drag forces (Cloete et al., 2018a). The 3-marker closure, where the drift GPM relies on gradients, also needs a large filter-to-grid-size ratio due to more diffuse solids structures (and therefore smaller gradients on average) in the coarse-grid simulations than in the filtered resolved simulation data used to the derive the closures. Since small drift GPM values will decrease the drag correction, the gradient-based 3-marker closure requires a larger filter-to-grid-size ratio to compensate for this effect (the interested reader can find more information in Chapter 5 of the thesis of Cloete (2018)).

3.3.1   Bubbling case

Figure 7 evaluates the performance of the fTFM with various closures in the bubbling case. In each panel, the case with the 2-marker anisotropic closure proposed in our previous study (Cloete et al., 2018a) and the resolved TFM results are shown as reference. Figure 7.a shows the importance of the fTFM closures, whereas Figure 7.b shows that the 2-marker isotropic closure tends to predict increasing bed expansion with increasing grid size. On the contrary, all three anisotropic closures show excellent grid independence in the bubbling case when considering bed expansion. An advantage of the 3-marker closure is unveiled on the coarsest grid (i.e., 40 mm, see Figure 7.d): this closure appears to successfully predict the smooth transition of the mean solids fraction near the interface, for which all other closures show oscillations. We note in passing that an earlier study (Cloete et al., 2017b) also verified the 3-marker anisotropic closure for bubbling fluidization in a partially-periodic domain. In this scenario, the 3-marker closure, in combination with a closure for the filtered reaction rate, also performed well in predicting reactive behaviour on a coarse grid.
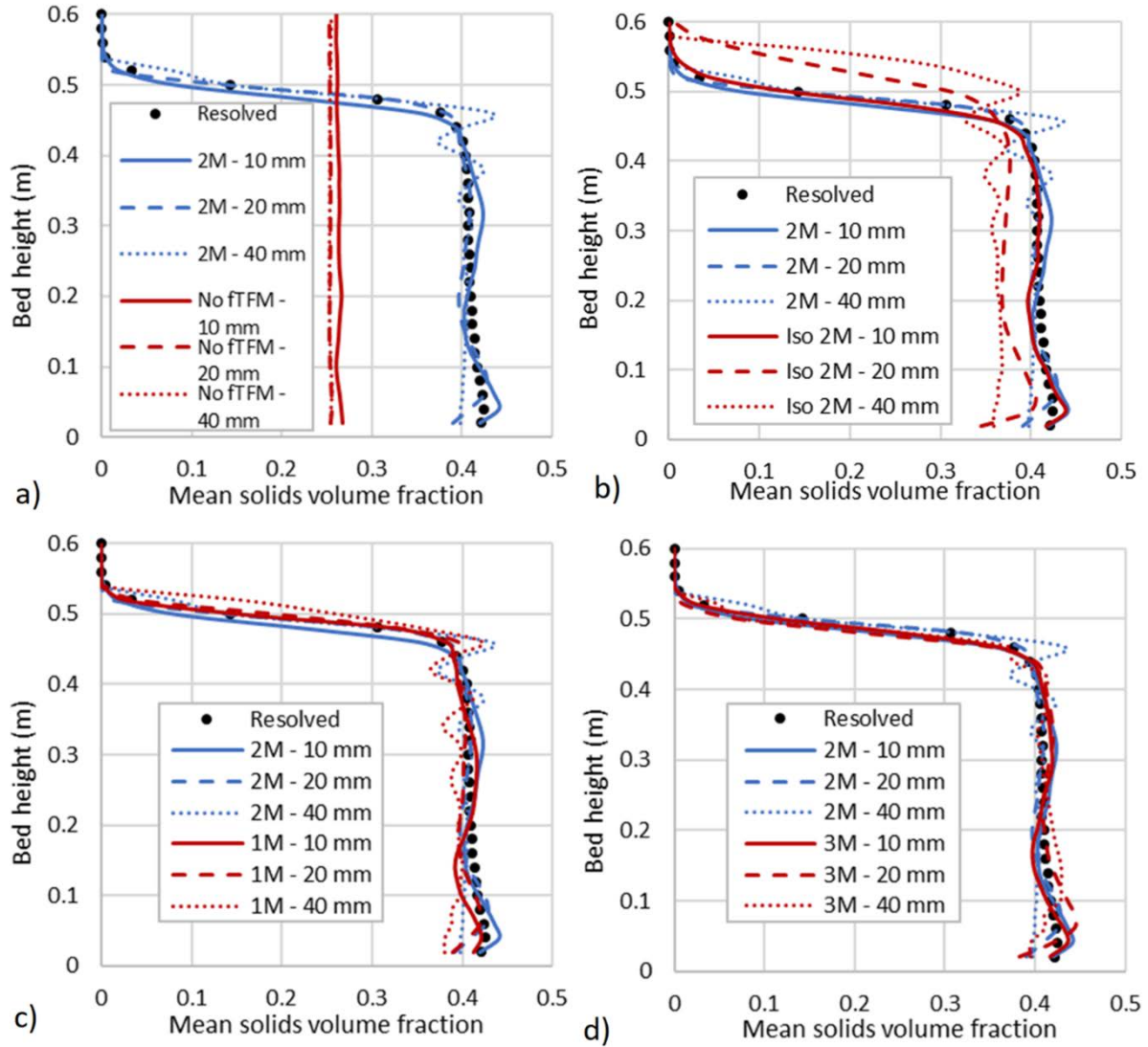
Figure 7 – Comparison of the time- and horizontally-averaged solids volume fraction as a function of the bed height for the 2-marker anisotropic closure (Case 1) with a) a case with no fTFM closures (Case 2), b) the 2-marker isotropic closure (Case 3), c) the 1-marker anisotropic closure (Case 4) and d) the 3-marker anisotropic closure (Case 5) for bubbling fluidization.

From the results in Figure 7, it is clear that the lateral drag plays an important role in the bubbling case. This can be confirmed by looking at an animation of the solids volume fraction contour plot of the resolved TFM simulation in the left panel of Video 1: it can be clearly seen that there are periods of significant horizontal movement of the gas bubbles. Comparing the two fTFM simulations on a 10 mm grid in Video 1, it is clear that the isotropic drag closure leads to a much stronger formation of lateral flow at the bottom of the bed, which extends almost completely to the left wall for most of the duration of the simulation. This behaviour does not match the fine-grid simulation well and is a consequence of the earlier finding that isotropic drag closures will substantially overpredict the drag in lateral directions (Cloete et al., 2018a). On the other hand, the anisotropic drag closure predicts behaviour of the lateral flow near the bottom of the bed that is more similar to that in the fine-grid TFM simulations: the lateral solids motion near the bottom of the bed is weaker and tends to fluctuate more.

It can further be noted that isotropic drag closures will increasingly overpredict the lateral drag with larger filter sizes (Cloete et al., 2018a). Therefore, since the filter-to-grid-size ratio was tuned for the isotropic drag closure to give the correct bed expansion on a 10 mm grid, this closure model cannot

compensate for the increasingly overpredicted lateral drag at larger grid sizes. This appears to indirectly lead to an increase of the overall vertical drag experienced by the solids with increasing grid size, since gas bubbles will tend to meander less. This explanation supports the observed grid dependency of the bed expansion when using the isotropic drag closure for bubbling beds (see Figure 7.b).
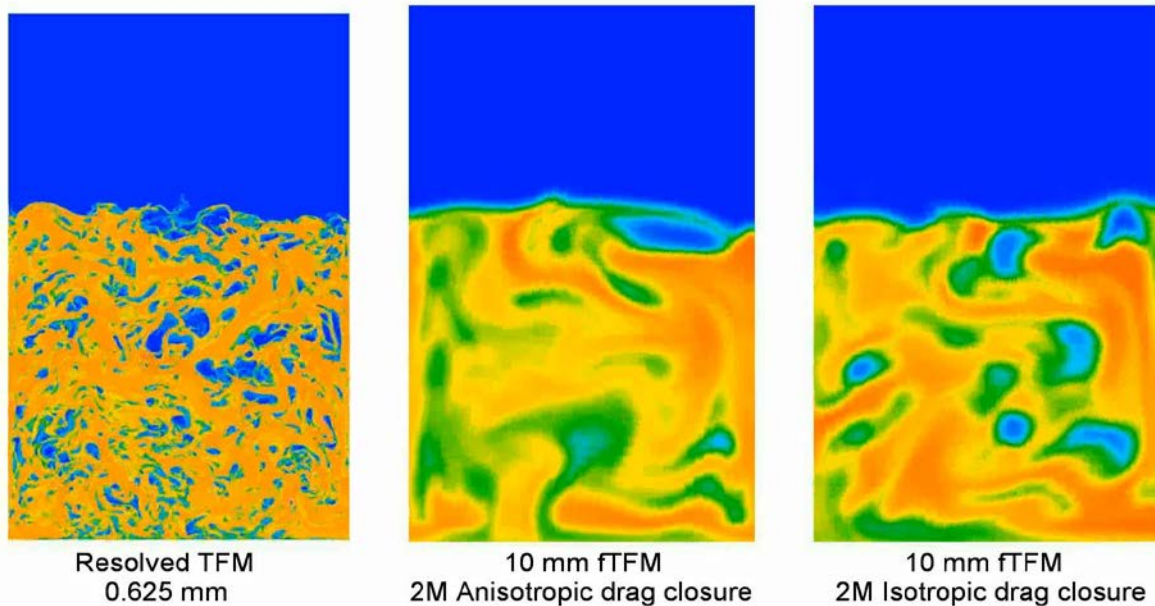
Video 1 – Animations of the solids volume fraction comparing the resolved TFM (left panel) to the fTFM with an anisotropic 2-marker drag closure (centre panel) and the fTFM with an isotropic 2-marker drag closure (right panel) on a 10 mm grid for the bubbling case. Blue corresponds to a solids volume fraction of 0 and red to a solids volume fraction of 0.6.

3.3.2   Turbulent case

Figure 8 evaluates the different fTFM formulations in the turbulent case. A prominent feature of the resolved TFM data is the relatively uniform bed density between heights of about 0.1 m and 0.4 m, followed by a gradual transition to a very dilute bed above a height of 0.7 m. From Figure 8.a, it can be seen that the anisotropic 2-marker closure is unable to predict this feature and instead predicts a steady decrease in solids volume fraction with increasing height. However, the overall bed expansion is only overpredicted slightly. Additionally, moderate grid dependency of the results can be seen for the 2-marker closure, with the bed expansion decreasing with increasing grid size. Nonetheless, the prediction remains reasonably good, especially when considering the case with no sub-grid modelling (Figure 8.a) for perspective.
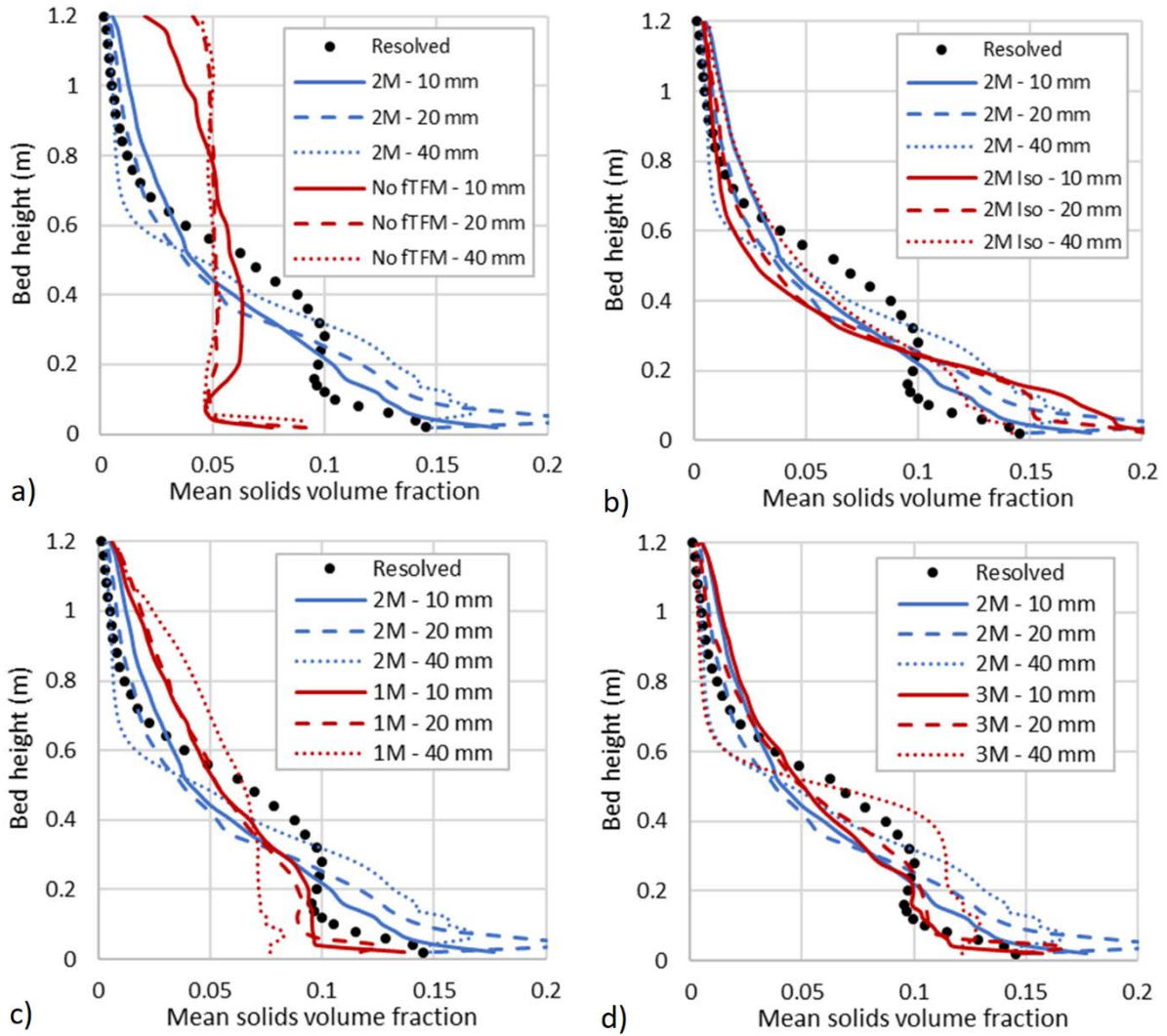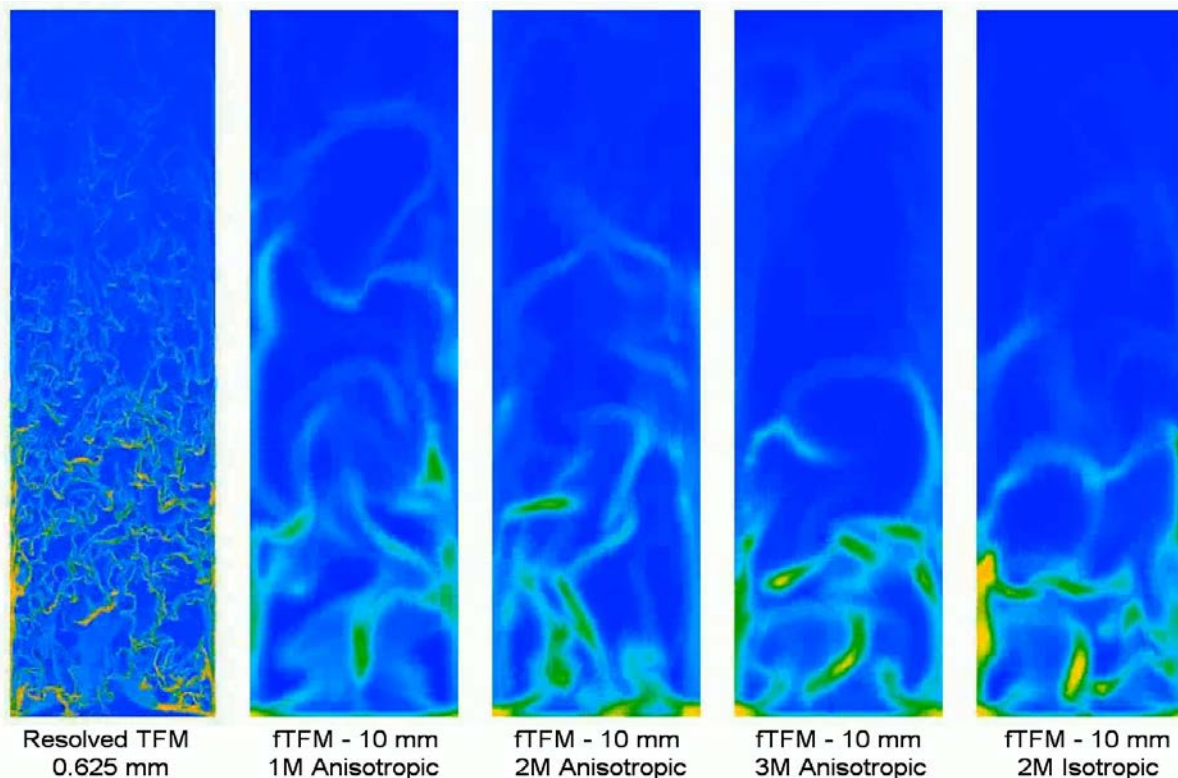
Figure 8 – Comparison of the time- and horizontally-averaged solids volume fraction as a function of the bed height for the 2-marker anisotropic closure (Case 1) with a) a case with no fTFM closures (Case 2), b) the 2-marker isotropic closure (Case 3), c) the 1-marker anisotropic closure (Case 4) and d) the 3-marker anisotropic closure (Case 5) for turbulent fluidization.

The isotropic 2-marker closure (Figure 8.b) shows the opposite behaviour to the anisotropic 2-marker closure. On the 10 mm grid, the bed expansion is significantly underpredicted, which can be explained as follows: in the bubbling case, the filter-to-grid-size ratio had to be increased to correctly predict the bed expansion, thereby artificially lowering the drag predicted by this closure, also in the vertical direction. However, in the turbulent case, lateral drag is less important than in the bubbling case. Consequently, the large filter-to-grid-size ratio now reduces the vertical drag too much, resulting in an underpredicted bed expansion of the isotropic closure on the 10 mm grid. As for grid dependence, the isotropic closure still shows the same trend as in the bubbling case, with increasing bed expansion observed with increasing grid size.

Considering the anisotropic 1-marker closures in Figure 8.c, it can be seen that this closure generally overpredicts the bed expansion in this case. A tentative explanation is that clustering is strongly affected by solids motion in turbulent beds, making it necessary to account for a typical velocity scale (and hence a second marker such as the filtered slip velocity) in addition to the filtered solids volume fraction. The performance of the 1-marker closure is comparable to that of the 2-marker closure, which overpredicts the bed density in the bottom of the bed in this case.

The 3-marker closure (see Figure 8.d), on the contrary, performs somewhat better than the other anisotropic closures in the turbulent case, since it manages to capture the region of uniform bed density around a height of 0.2 m, at least to some degree. However, it predicts the same slight overexpansion of the bed as the 2-marker closure. Grid independence is good from 10 mm to 20 mm for the 3-marker closure. However, the bed expansion significantly decreases when going to 40 mm, although it still captures the uniform volume fraction region better than the 2-marker closure. In general, it can therefore be concluded that increasing the number of markers in the anisotropic filtered drag force closure leads to some improvement to the coarse-grid simulations predictions in the turbulent case.

The behaviour in the turbulent case is qualitatively shown in Video 2. The fTFM simulations are shown on the 10 mm grid, where all the closures should be most accurate since the least amount of sub-grid modelling is required. For the resolved TFM, it can be seen that, in the bottom half of the bed, relatively dense clusters rise in the centre, whereas lower density clusters are generally falling in the top half. These clusters tend to collide in the middle of the bed, which seems to be the cause of the relatively sudden change in mean volume fraction observed in Figure 8. In general, the anisotropic closures have some difficulty capturing this behaviour. However, the results in Figure 8, and a careful evaluation of Video 2, tentatively indicates an improvement of the prediction with increasing closure complexity of the anisotropic closure. Finally, the isotropic 2-marker closure clearly overpredicts the holdup in the bottom of the bed, which is likely partly due to the large filter-to-grid ratio required in the bubbling case for this closure. The animation reveals an additional reason for this behaviour of the isotropic closure: in the bottom of the bed, the overpredicted lateral drag force causes clusters to move in the lateral direction, and to rapidly collide with each other, or with the walls. We speculate that this mechanism leads to the formation of unrealistically large and dense clusters that are more difficult to convey upwards with the fluidizing gas.

| Resolved TFM | fTFM - 10 mm | fTFM - 10 mm | fTFM - 10 mm | fTFM - 10 mm |
| 0.625 mm | 1M Anisotropic | 2M Anisotropic | 3M Anisotropic | 2M Isotropic |

Video 2 – Animations of the solids volume fraction comparing the resolved TFM with fTFM simulations on a 10 mm grid in the turbulent case. From the left to right the panels show: the resolved TFM, the 1-marker anisotropic closure, the 2-marker

3.3.3   Core-annular case

From Figure 9.a, it can be seen that the anisotropic 2-marker closure performs quite well in the core-annular case, with good predictions at the very bottom and upper parts of the bed. Only a slightly too dense region between a height of 0.1 m and 0.4 m is predicted. However, the 40 mm grid generally underpredicts the solids holdup in the bed. In contrast, the isotropic 2-marker closure (Figure 9.b) greatly overpredicts the solids holdup in general. Similar to the turbulent case, this is due to the large filter-to-grid-size ratio required for this closure to match resolved TFM data of bed expansion for the bubbling case (where the horizontal drag played a significant role). Since the core-annular domain is narrower than the turbulent domain, the horizontal drag becomes even less influential. Consequently, this leads to the conclusion that the excessively large filter-to-grid-size ratio (that is rooted in the bubbling case results) causes an extreme underprediction of the drag by the isotropic closure.
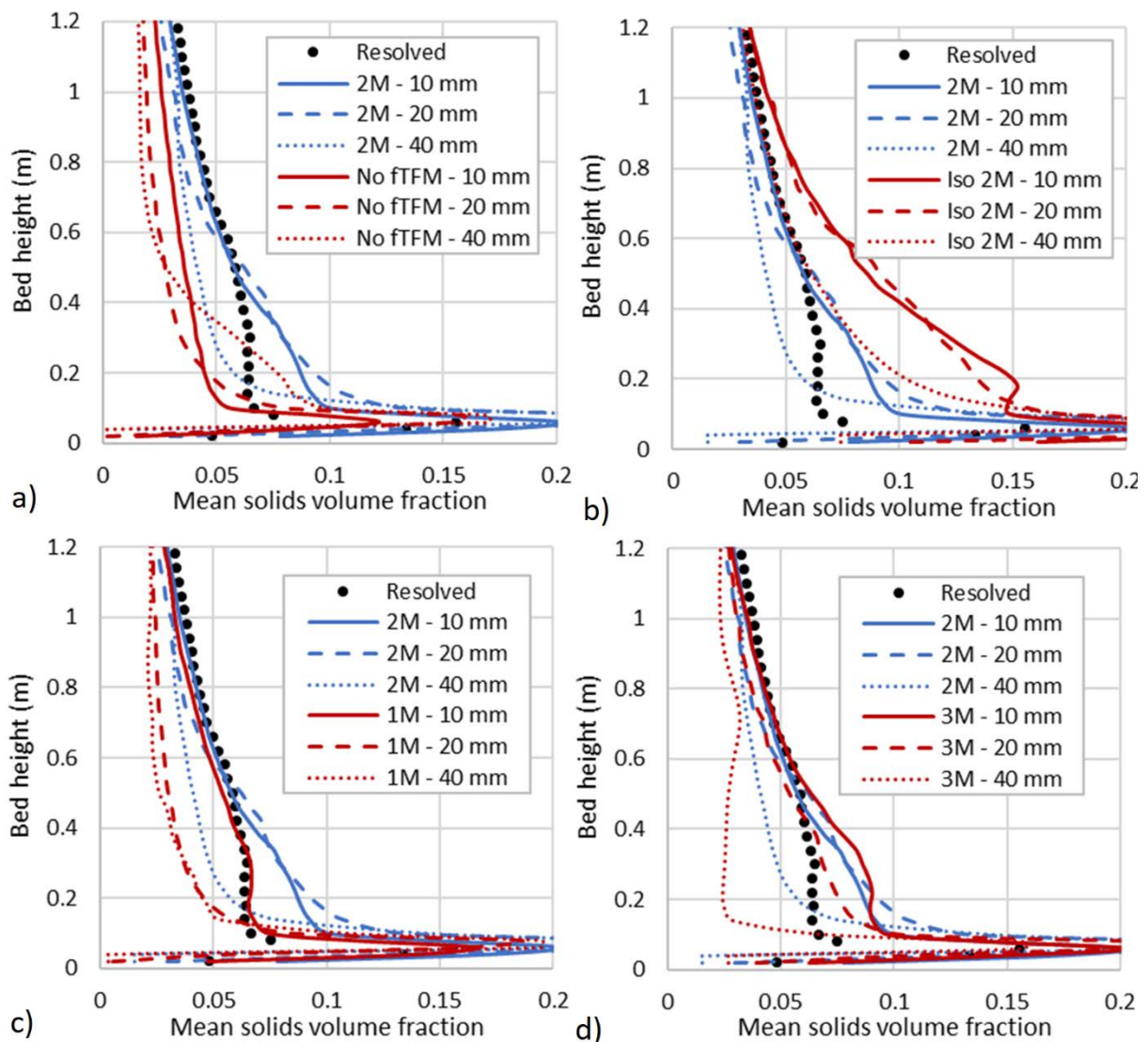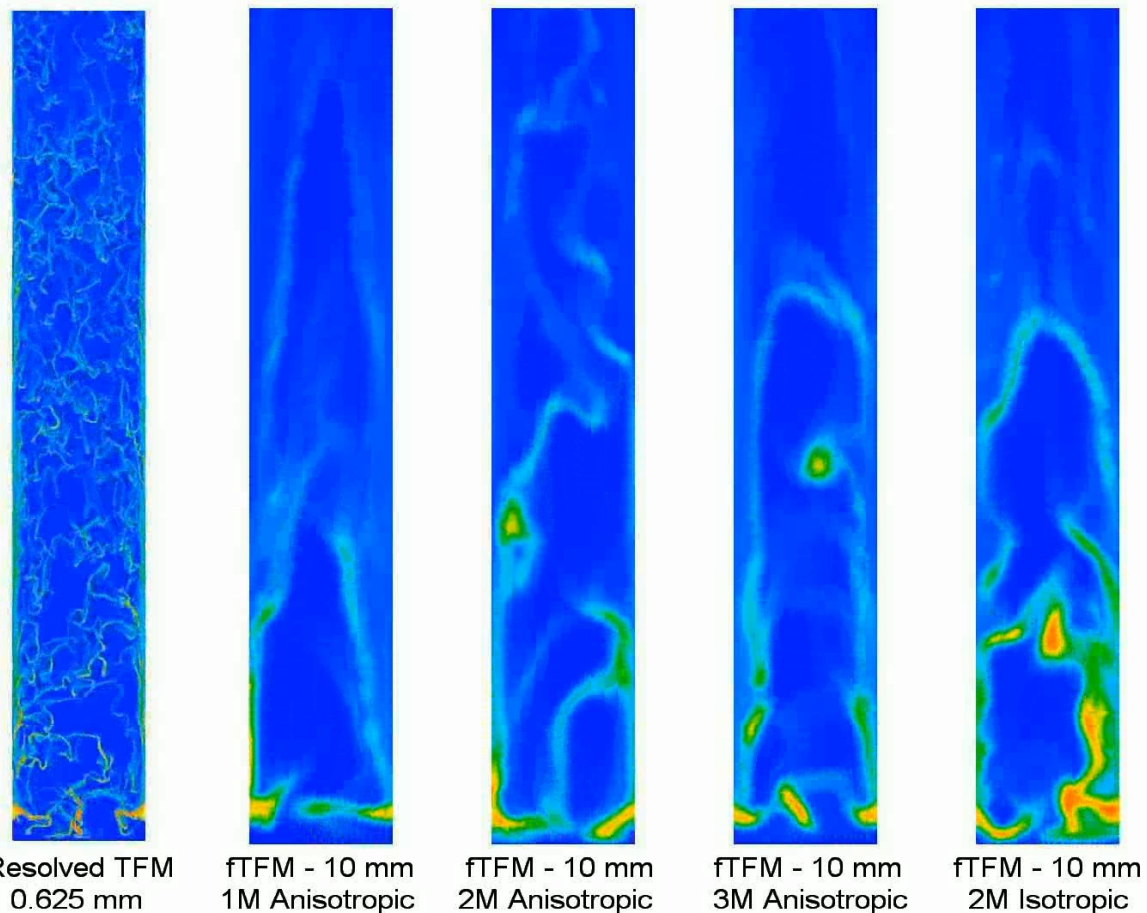

Figure 9 – Comparison of the time- and horizontally-averaged solids volume fraction as a function of the bed height for the 2-marker anisotropic closure (Case 1) with a) a case with no fTFM closures (Case 2), b) the 2-marker isotropic closure (Case 3), c) the 1-marker anisotropic closure (Case 4) and d) the 3-marker anisotropic closure (Case 5) for fluidization in the core-annular regime.

Surprisingly, the 1-marker anisotropic closure (Figure 9.c) shows nearly an exact match to the resolved TFM data in the 10 mm case. However, this might be coincidental, since the 1-marker model significantly overpredicts the drag in the turbulent case and at the other two grid sizes for the core-annular case. Although the prediction of the 3-marker anisotropic closure (see Figure 9.d) is reasonable for the 10 mm and 20 mm cases, it still shows an overprediction of the bed density in the lower part of the bed (for the 10 mm grid, this overprediction of the 3-marker closure is slightly larger than that of the 2-marker closure). Furthermore, the 3-marker closure features a significant grid dependency when going from 10 mm to 20 mm. Also, the solids holdup is strongly underpredicted in the 40 mm case. It therefore appears that, contrary to the turbulent case, the 3-marker anisotropic closure actually performs somewhat worse than the anisotropic 2-marker closure in the core-annular regime of fluidization.

Therefore, considering all three verification cases, a clear improvement of the 3-marker closure over the 2-marker closure cannot be seen. This is possibly related to the results of the *a priori* analysis in section 3.2, which showed that for the large filter sizes considered here (keeping in mind that a filter-to-grid-size ratio of 1.8 is employed for the 3-marker closure), adding the drift GPM as a third marker did not significantly affect the predictive capability of the closure in the vertical direction. This is likely related to the fact that the flow gradients become small at large filter sizes, meaning that the effect of the GPM becomes small compared to that of the gravitational contribution in the vertical direction.

A qualitative comparison of the resolved TFM to the fTFM with different drag closures on the 10 mm grid is shown in Video 3. The resolved TFM shows that, as solids accumulate near the ports located at the walls near the gas inlet, the gas rising in the centre shears off solids clusters. These clusters are then swept upwards and are dispersed. The gas then pushes some of the solids towards the walls, where particles accumulate and fall down. This behaviour is reasonably captured by the anisotropic closures, but the amount of solids accumulating at the walls in the lower part of the bed increases as the complexity of the anisotropic drag closure increases, leading to an overprediction of the solids holdup in the lower region of the bed. The reason for this is unclear, since the *a priori* analysis in section 3.2 shows that the predictive capability of the fTFM should increase with an increasing number of markers in the filtered drag force closure. Relative to the anisotropic closures, Video 3 shows that the isotropic closure predicts much too large and dense solids clusters in the coarse-grid simulations of the core-annular case near the bottom of the bed. This is due to the underprediction of the drag caused by the large grid-to-filter-size ratio required to match fine-grid simulations in the bubbling regime.

| Resolved TFM | fTFM - 10 mm | fTFM - 10 mm | fTFM - 10 mm | fTFM - 10 mm |
| 0.625 mm | 1M Anisotropic | 2M Anisotropic | 3M Anisotropic | 2M Isotropic |

Video 3 – Animations of the solids volume fraction comparing the resolved TFM to fTFM simulations on a 10 mm grid in the core-annular case. From the left to right the panels show: the resolved TFM, the 1-marker anisotropic closure, the 2-marker anisotropic closure, the 3-marker anisotropic closure and the 2-marker isotropic closure. Blue corresponds to a solids volume fraction of 0 and red to a solids volume fraction of 0.6.

Finally, Video 4 shows the effect of the grid size on the behaviour of the fTFM in the core-annular case when using the anisotropic 2-marker closure for the filtered drag force. Increasing grid size clearly affects the predicted mechanism by which solids are removed near the ports, since the clusters that are sheared off can no longer be resolved on the larger grid sizes. This has an especially large effect when considering the 40 mm grid, where all the fTFM closures show a large drop in solids holdup in Figure 9. On this grid, dense solids clusters, which are more difficult to fluidize, can no longer be directly predicted by the fTFM. It can be noted that the grid size of 40 mm is the same as the width of the inlet ports for the solids and that only 6 cells span the width of the domain. Much of the grid dependency observed for the core-annular case can therefore be attributed to the grid size becoming too large to resolve important macroscopic flow features. It may therefore be deduced that the macroscopic flow features will put a limit on the maximum grid size that may be used for a specific case, regardless of the quality of the fTFM closures that are used. It may also be speculated that the fact that the grid is too coarse to resolve macroscopic flow effects introduces uncertainty in the comparisons of the present study and may be the reason why improved performance of the 3-marker closure over the 2-marker closure cannot be established in the *a posteriori* analysis, despite the *a priori* analysis showing that minor improvements may be expected.

Resolved TFM   fTFM - 10 mm   fTFM - 20 mm   fTFM - 40 mm
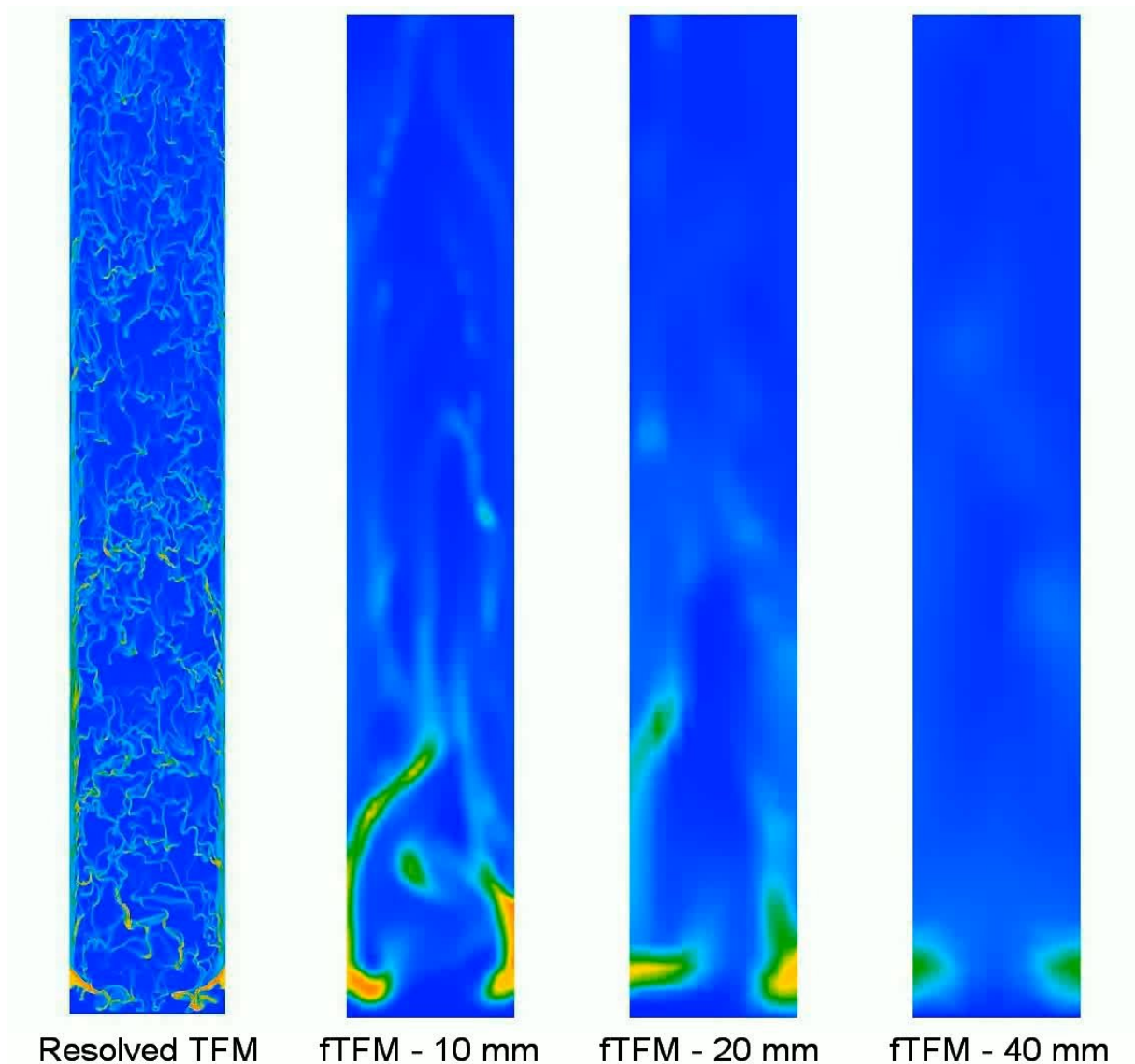
Video 4 - Animations of the solids volume fraction showing the grid dependence of the fTFM simulations in the core-annular case with the 2-marker anisotropic closure for the filtered drag force. From the left to right the panels show: the resolved TFM, the fTFM on a 10 mm grid, the fTFM on a 20 mm grid and the fTFM on a 40 mm grid. Blue corresponds to a solids volume fraction of 0 and red to a solids volume fraction of 0.6.

4   Conclusions and recommendations

In the present study, anisotropic closures of increasing complexity were derived for the filtered drag force, which is generally considered as the most important closure in fTFMs. Significant improvements with increasing closure complexity were difficult to distinguish with certainty in the *a posteriori* analysis, except for a minor tendency of the simplest 1-marker closure to overestimate the drag in fast and dilute flows. In contrast, an isotropic closure from a previous study (Cloete et al., 2018a) showed substantially more grid dependence in the bubbling case and much poorer generality over all the cases. This is due to the tendency of isotropic filtered drag force closures to drastically overpredict the filtered drag force in the lateral direction, as discussed in a previous study (Cloete et al., 2018a). These findings are in line with the *a priori* study, which showed relatively small improvements when increasing the complexity of anisotropic drag closures, compared to clear benefits when going from an isotropic closure to an anisotropic closure.

The results of this study therefore suggest that it is essential to account for anisotropy when considering drag closures for fTFMs intended for use on very coarse grids. It should be noted that the quantitative importance of the anisotropy observed in the drag correction from 2D simulations presented here may be different in 3D, since gas would more easily slip around solids clusters. Future work is therefore recommended to investigate this by validating the anisotropic drag closure presented here against 3D experimental data and by considering filtered data from fine-grid 3D TFM simulations.

Despite this uncertainty, the results of the present paper yield an important conclusion by verifying closures of varying complexity in 2D: that it is critical that fTFM closures account for important physical effects, such as anisotropy, but that extremely complex closures may not be necessary. It is therefore recommended that future research should aim to find, and include, such physical effects that are missing from current fTFM closures. Theoretical considerations, similar to the work of Schneiderbauer (2017) may be important to assist in this process.

Two further findings from the present study have important implications for future fTFM studies. Firstly, it appears that even larger resolved simulations than those afforded by 2D simulations in the present study are required for detailed verification of fTFM closures at large filter sizes. This is since uncertainty is introduced when the coarse-grid simulations cannot resolve important macro-scale flow features such as concentrated solids injections and solids circulation patterns. Such large simulation domains would be especially problematic for 3D simulations, considering that the 2D simulations of the present study already required 1-2 months of simulation time on 256 HPC cores each, and 3D simulations would require 2-4 orders of magnitude more computational time.

The second important finding is that the optimal filter-to-grid-size ratio for a specific fTFM depends on the formulation of closures and the chosen markers. This implies that in *a posteriori* tests, the optimal filter-to-grid-size ratio should be determined for a specific fTFM to be tested, in order to ensure a fair comparison between different model formulations. This finding also introduces uncertainty in the use of the fTFM, for example when closures for different filtered quantities use different marker types. Further research is suggested to better understand this topic.

Finally, despite the good performance reported here, considering the very large grid cells and wide range of fluidization conditions considered in the verification, several shortcomings of the approach followed in this study can be noted. In the present study, a functional fitting approach was employed, as common in the fTFM literature (Gao et al., 2018; Igci et al., 2008; Sarkar et al., 2016; Schneiderbauer and Pirker, 2014). In such an approach, correlations, based on several markers (independent variables), are fitted to filtered quantities obtained from resolved TFM simulations. This study reveals two challenges of using this approach: 1) additional independent variables may be added without leading to substantial improvements in *a posteriori* tests and 2) a large number of model coefficients may have to be tuned in such closures. Another challenge, although not specifically addressed in the present study, is concerned with accounting for different fluid and particle properties in the closures. Literature (Schneiderbauer and Pirker, 2016) indicates that the scalings that are commonly used in fTFM closures to account for different fluid/particle configurations may not be very accurate. However, this topic has received relatively little attention, mainly due to the complexity of including data from many different particle/fluid configurations in the functional fitting process.

Stronger use of theoretical arguments in the development of fTFM closures, e.g. algebraic closures for sub-grid quantities based on transport equations (Schneiderbauer, 2017) or dynamic adaption procedures (Ozel et al., 2013; Ozel et al., 2017; Parmentier et al., 2012), may help to address the

challenges that have been listed. These possibilities will be explored in future studies to further strengthen the fTFM developed here.

5   Acknowledgements

6   List of Acronyms and Symbols

Acronym definitions:

CFD   Computational Fluid Dynamics

EMMS   Energy-minimization Multi-scale

fTFM   Filtered Two-fluid Model

GPM   Gradient Product Marker

KTGF   Kinetic Theory of Granular Flow

TFM   Two Fluid Model

UDF   User-defined function

Main Symbol definitions:

C_{NL} Non-linearity correction factor

d_p Particle diameter (m)

$\vec{g}$ Gravity vector (m/s^2)

K_{gs} Interphase momentum exchange coefficient (kg/(m^3.s))

k_{Θ_s} Granular temperature diffusion coefficient (kg/(m.s))

p Pressure (Pa)

t Time (s)

v_t Particle terminal velocity (m/s)

α Volume fraction

ϕ_{gs} Interphase energy transfer (W/m^3)

γ_{Θ_s} Dissipation rate (W/m^3)

M   Gradient product marker (m^{-2})

μ Dynamic viscosity (kg/(m.s))

ρ Density (kg/m^3)

$\bar{\bar{\tau}}$ Stress tensor (Pa)

υ Velocity (m/s)

Δ_f Filter size (m)

Θ Granular temperature (m^2/s^2)

Sub- and superscript definitions:

adj Adjusted slip

d Drift

fil Filter

g Gas

hom Homogenous

k Generic phase

i Coordinate index

s Solid

Operator definitions

$|x|$ Absolute values

$\bar{x}$ Algebraic volume average

x', x'' Fluctuation from mean

$\hat{x}$ Non-dimensionalized value

$\tilde{x}$ Phase-weighted volume average

x^* Scaled value

$\vec{x}$ Vector quantity

7 Appendix

The derivation of the new definition of the drift velocity presented in section 3.1.3 is detailed in this section, starting with the definition of the filtered drag force.

$$\overline{K_{gs}(v_{g,\iota} - v_{s,\iota})}$$

$$= \frac{\overline{K_{gs}}}{\alpha_s}(\alpha_s v_{g,\iota} - \alpha_s v_{s,\iota})$$

$$= C_1 \overline{K_{gs}} \frac{\overline{(\alpha_s v_{g,\iota} - \alpha_s v_{s,\iota})}}{\bar{\alpha}_s} \qquad\qquad C_1 = \frac{\overline{\frac{K_{gs}}{\alpha_s}}(\alpha_s v_{g,\iota} - \alpha_s v_{s,\iota})}{\overline{K_{gs}}\frac{\overline{(\alpha_s v_{g,\iota} - \alpha_s v_{s,\iota})}}{\bar{\alpha}_s}}$$

$$= C_1 C_2 K_{gs,hom} \frac{\overline{(\alpha_s v_{g,\iota} - \alpha_s v_{s,\iota})}}{\bar{\alpha}_s} \qquad\qquad C_2 = \frac{\overline{K_{gs}}}{K_{gs,hom}}$$

$$= C_{NL} K_{gs,hom}(\frac{\overline{\alpha_s v_{g,\iota}}}{\bar{\alpha}_s} - \frac{\overline{\alpha_s v_{s,\iota}}}{\bar{\alpha}_s}) \qquad\qquad C_{NL} = C_1 C_2$$

$$= C_{NL} K_{gs,hom}(\frac{\overline{\alpha_s v_{g,\iota}}}{\bar{\alpha}_s} - \tilde{v}_{s,i})$$

$$= C_{NL} K_{gs,hom}(\frac{\overline{(1 - \alpha_g)v_{g,\iota}}}{\bar{\alpha}_s} - \tilde{v}_{s,i})$$

$$= C_{NL} K_{gs,hom}(\frac{\bar{v}_{g,i} - \overline{\alpha_g v_{g,\iota}}}{\bar{\alpha}_s} - \tilde{v}_{s,i})$$

$$= C_{NL} K_{gs,hom}(\frac{\bar{v}_{g,i}}{\bar{\alpha}_s} - \frac{\bar{\alpha}_g \tilde{v}_{g,i}}{\bar{\alpha}_s} - \tilde{v}_{s,i})$$

We now consider:

$$\tilde{v}_{g,i} = \frac{\overline{\alpha_g v_{g,\iota}}}{\bar{\alpha}_g} = \frac{\overline{(\bar{\alpha}_g + \alpha_g')(\overline{v_{g,\iota}} + v_{g,\iota}')}}{\bar{\alpha}_g} = \frac{\overline{\bar{\alpha}_g}\,\overline{v_{g,\iota}} + \overline{\alpha_g' v_{g,\iota}'}}{\bar{\alpha}_g} = \overline{v_{g,\iota}} + \frac{\overline{\alpha_g' v_{g,\iota}'}}{\bar{\alpha}_g}$$

Which leads to:

$$\overline{v_{g,\iota}} = \tilde{v}_{g,i} - \frac{\overline{\alpha_g' v_{g,\iota}'}}{\bar{\alpha}_g}$$

Then,

$$C_{NL} K_{gs,hom}(\frac{\bar{v}_{g,i}}{\bar{\alpha}_s} - \frac{\bar{\alpha}_g \tilde{v}_{g,i}}{\bar{\alpha}_s} - \tilde{v}_{s,i})$$

$$= C_{NL} K_{gs,hom}(\frac{\tilde{v}_{g,i} - \overline{\alpha_g' v_{g,\iota}'}/\bar{\alpha}_g}{\bar{\alpha}_s} - \frac{\bar{\alpha}_g \tilde{v}_{g,i}}{\bar{\alpha}_s} - \tilde{v}_{s,i})$$

$$= C_{NL} K_{gs,hom}(\frac{(1 - \bar{\alpha}_g)\tilde{v}_{g,i}}{\bar{\alpha}_s} - \frac{\overline{\alpha_g' v_{g,\iota}'}}{\bar{\alpha}_s \bar{\alpha}_g} - \tilde{v}_{s,i})$$

$$= C_{NL} K_{gs,hom}(\tilde{v}_{g,i} - \tilde{v}_{s,i} - \frac{\overline{\alpha_g' v_{g,\iota}'}}{\bar{\alpha}_s \bar{\alpha}_g})$$

Therefore,

$$v_{d,i} = \frac{\overline{\alpha'_g v'_{g,i}}}{\bar{\alpha}_s \bar{\alpha}_g}$$

8 References

Bakshi, A., Altantzis, C., Bates, R.B., Ghoniem, A.F., 2016. Study of the effect of reactor scale on fluidization hydrodynamics using fine-grid CFD simulations based on the two-fluid model. Powder Technology 299, 185-198.

Bi, H.T., Grace, J.R., 1995. Flow regime diagrams for gas-solid fluidization and upward transport. International Journal of Multiphase Flow 21, 1229-1236.

Cloete, J.H., 2018. Development of Anisotropic Filtered Two Fluid Model Closures, Department of Energy and Process Technology. Norwegian University of Science and Technology, Trondheim, Norway.

Cloete, J.H., Cloete, S., Municchi, F., Radl, S., Amini, S., 2017a. The sensitivity of filtered Two Fluid Model to the underlying resolved simulation setup. Powder Technology 316, 265-277.

Cloete, J.H., Cloete, S., Municchi, F., Radl, S., Amini, S., 2018a. Development and verification of anisotropic drag closures for filtered Two Fluid Models. Chemical Engineering Science 192, 930-954.

Cloete, J.H., Cloete, S., Radl, S., Amini, S., 2016a. Evaluation of wall friction models for riser flow. Powder Technology 303, 156-167.

Cloete, J.H., Cloete, S., Radl, S., Amini, S., 2017b. Verification study of anisotropic filtered Two Fluid Model Closures, AIChE Annual Meeting, Minneapolis, USA.

Cloete, J.H., Cloete, S., Radl, S., Amini, S., 2018b. Development and verification of anisotropic solids stress closures for filtered Two Fluid Models. Chemical Engineering Science 192, 906-929.

Cloete, S., Amini, S., Johansen, S.T., 2011. On the effect of cluster resolution in riser flows on momentum and reaction kinetic interaction. Powder Technology 210, 6-17.

Cloete, S., Cloete, J.H., Amini, S., 2016b. Comparison of the Filtered Two Fluid Model and Dense Discrete Phase Model for Large-Scale Fluidized Bed Reactor Simulations, AIChE Annual Meeting San Franciso, USA.

Cloete, S., Cloete, J.H., Amini, S., 2018c. Hydrodynamic validation study of filtered Two Fluid Models. Chemical Engineering Science 182, 93-107.

Cloete, S., Johansen, S.T., Amini, S., 2015a. Grid independence behaviour of fluidized bed reactor simulations using the Two Fluid Model: Effect of particle size. Powder Technology 269, 153-165.

Cloete, S., Johansen, S.T., Amini, S., 2016c. Grid independence behaviour of fluidized bed reactor simulations using the Two Fluid Model: Detailed parametric study. Powder Technology 289, 65-70.

Cloete, S., Johansen, S.T., Zaabout, A., van Sint Annaland, M., Gallucci, F., Amini, S., 2015b. The effect of frictional pressure, geometry and wall friction on the modelling of a pseudo-2D bubbling fluidised bed reactor. Powder Technology 283, 85-102.

Cloete, S., Zaabout, A., Johansen, S.T., van Sint Annaland, M., Gallucci, F., Amini, S., 2013. The generality of the standard 2D TFM approach in predicting bubbling fluidized bed hydrodynamics. Powder Technology 235, 735-746.

Ellis, N., Xu, M., Lim, C.J., Cloete, S., Amini, S., 2011. Effect of Change in Fluidizing Gas on Riser Hydrodynamics and Evaluation of Scaling Laws. Industrial & Engineering Chemistry Research 50, 4697-4706.

Gao, X., Li, T., Sarkar, A., Lu, L., Rogers, W.A., 2018. Development and validation of an enhanced filtered drag model for simulating gas-solid fluidization of Geldart A particles in all flow regimes. Chemical Engineering Science 184, 33-51.

Gidaspow, D., Bezburuah, R., Ding, J., 1992. Hydrodynamics of Circulating Fluidized Beds, Kinetic Theory Approach, 7th Engineering Foundation Conference on Fluidization pp. 75-82.

Hamidouche, Z., Masi, E., Fede, P., Simonin, O., Mayer, K., Penthor, S., 2019. Unsteady three-dimensional theoretical model and numerical simulation of a 120-kW chemical looping combustion pilot plant. Chemical Engineering Science 193, 102-119.

Huilin, L., Gidaspow, D., 2003. Hydrodynamics of binary fluidization in a riser: CFD simulation using two granular temperatures. Chemical Engineering Science 58, 3777-3792.

Igci, Y., Andrews, A.T., Sundaresan, S., Pannala, S., O'Brien, T., 2008. Filtered two-fluid models for fluidized gas-particle suspensions. AIChE Journal 54, 1431-1448.

Igci, Y., Sundaresan, S., 2011. Constitutive Models for Filtered Two-Fluid Models of Fluidized Gas–Particle Flows. Industrial & Engineering Chemistry Research 50, 13190-13201.

Jiang, Y., Kolehmainen, J., Gu, Y., Kevrekidis, Y.G., Ozel, A., Sundaresan, S., 2018. Neural-network-based filtered drag model for gas-particle flows. Powder Technology.

Johnson, P.C., Jackson, R., 1987. Frictional-Collisional Constitutive Relations for Granular Materials, with Application to Plane Shearing. Journal of Fluid Mechanics 176, 67-93.

Leonard, B.P., Mokhtari, S., 1990. ULTRA-SHARP Nonoscillatory Convection Schemes for High-Speed Steady Multidimensional Flow, NASA TM 1-2568 (ICOMP-90-12), NASA Lewis Research Center.

Lun, C.K.K., Savage, S.B., Jeffrey, D.J., Chepurniy, N., 1984. Kinetic Theories for Granular Flow: Inelastic Particles in Couette Flow and Slightly Inelastic Particles in a General Flow Field. Journal of Fluid Mechanics 140, 223-256.

Luo, H., Lu, B., Zhang, J., Wu, H., Wang, W., 2017. A grid-independent EMMS/bubbling drag model for bubbling and turbulent fluidization. Chemical Engineering Journal 326, 47-57.

Milioli, C.C., Milioli, F.E., Holloway, W., Agrawal, K., Sundaresan, S., 2013. Filtered two-fluid models of fluidized gas-particle flows: New constitutive relations. AIChE Journal 59, 3265-3275.

Municchi, F., Goniva, C., Radl, S., 2016. Highly efficient spatial data filtering in parallel using the opensource library CPPPO. Computer Physics Communications 207, 400-414.

Ostermeier, P., Vandersickel, A., Gleis, S., Spliethoff, H., 2017. Three dimensional multi fluid modeling of Geldart B bubbling fluidized bed with complex inlet geometries. Powder Technology 312, 89-102.

Ozel, A., Fede, P., Simonin, O., 2013. Development of filtered Euler–Euler two-phase model for circulating fluidised bed: High resolution simulation, formulation and a priori analyses. International Journal of Multiphase Flow 55, 43-63.

Ozel, A., Gu, Y., Milioli, C.C., Kolehmainen, J., Sundaresan, S., 2017. Towards filtered drag force model for non-cohesive and cohesive particle-gas flows. Physics of Fluids 29, 103308.

Parmentier, J.-F., Simonin, O., Delsart, O., 2012. A functional subgrid drift velocity model for filtered drag prediction in dense fluidized bed. AIChE Journal 58, 1084-1098.

Patankar, S., 1980. Numerical Heat Transfer and Fluid Flow. Hemisphere Publishing Corporation.

Pope, S.B., 2000. Tubulent Flows. Cambridge University Press, Cambridge, UK.

Sarkar, A., Milioli, F.E., Ozarkar, S., Li, T., Sun, X., Sundaresan, S., 2016. Filtered sub-grid constitutive models for fluidized gas-particle flows constructed from 3-D simulations. Chemical Engineering Science 152, 443-456.

Schaeffer, D.G., 1987. Instability in the Evolution Equations Describing Incompressible Granular Flow. Journal of Differential Equations 66, 19-50.

Schneiderbauer, S., 2017. A spatially-averaged two-fluid model for dense large-scale gas-solid flows. AIChE Journal 63, 3544-3562.

Schneiderbauer, S., Pirker, S., 2014. Filtered and heterogeneity-based subgrid modifications for gas–solid drag and solid stresses in bubbling fluidized beds. AIChE Journal 60, 839-854.

Schneiderbauer, S., Pirker, S., 2016. The impact of different fine grid simulations on the sub-grid modification for gas–solid drag, 9th International Conference on Multiphase Flow, Firenze.

Schneiderbauer, S., Saeedipour, M., 2018. Approximate deconvolution model for the simulation of turbulent gas-solid flows: An a priori analysis. Physics of Fluids 30, 023301.

Tricomi, L., Melchiori, T., Chiaramonti, D., Boulet, M., Lavoie, J.M., 2017. Sensitivity Analysis and Accuracy of a CFD-TFM Approach to Bubbling Bed Using Pressure Drop Fluctuations. Frontiers in Bioengineering and Biotechnology 5.

Wang, W., Li, J., 2007. Simulation of gas-solid two-phase flow by a multi-scale CFD approach-of the EMMS model to the sub-grid level. Chemical Engineering Science 62, 208-231.

Yang, N., Wang, W., Ge, W., Wang, L., Li, J., 2004. Simulation of Heterogeneous Structure in a Circulating Fluidized-Bed Riser by Combining the Two-Fluid Model with the EMMS Approach. Industrial & Engineering Chemistry Research 43, 5548-5561.